

WORCESTER POLYTECHNIC INSTITUTE

# Direct Ink Write Strain Sensors for Continuum Robotics

by

Daniel Charles Moyer

A thesis submitted in partial fulfillment for the  
degree of Master of Science

in

Mechanical Engineering

April 2024

APPROVED:

---

Professor Pratap Rao

---

Professor Loris Fichera

---

Professor Yihao Zheng

# Table of Contents

Abstract.....	3
Chapter 1. Introduction.....	4
1.1 Literature Review and Knowledge Gap.....	7
1.2 Objectives and Scope.....	9
Chapter 2. Printing and Characterization of Behavior of Printed Strain Sensors.....	11
2.1 Methods and Materials.....	15
2.2 Results.....	19
2.3 Discussion.....	29
2.4 Conclusion.....	31
Chapter 3. Integrating Printed Strain Sensor on CAAR.....	32
3.1 Methods and Materials.....	32
3.2 Results.....	34
3.3 Discussion.....	35
3.4 Conclusion.....	37
Chapter 4. Integrating Printed Strain Sensor on NWT.....	38
4.1 Methods and Materials.....	39
4.2 Results.....	40
4.3 Discussion.....	41
4.4 Conclusion.....	42
Chapter 5. Broader Impacts.....	43
Chapter 6. Conclusion.....	46
References.....	48

## Abstract

The growing field of soft and continuum robotics requires new types of strain sensors that are stretchable, flexible, and can function at much higher strains than traditional strain gauges can handle. Sensors made of three different stretchable conductive materials (silver-polymer composite, carbon-polymer composite, and liquid metal composite) were printed using direct ink write onto stretchable thermoplastic polyurethane films. The response of the sensors was evaluated over a period of cyclic stretching under different strain, speed, and dwell conditions, and evaluated in terms of gauge factor, linearity, and drift. The results show that the silver-based sensor material has high drift, a gauge factor of between 1.75 and 21.06, and a linearity of between 82.4% and 99.63%. The carbon-based material has a slightly negative drift, a linearity of between 96.71% and 98.51%, and a gauge factor of between 1.65 and 3.69. The liquid metal-based material has low drift, a linearity of 99.8%, and a gauge factor of between 0.75 and 1.03. Based on these results, the printed liquid metal-based sensor was chosen for integration with two continuum robots, namely a 3D-printed concentric agonist-antagonist robot (CAAR) and a metal shape memory alloy notched wrist tube (NWT), by adhering the sensor onto the robot bodies. The printed liquid metal-based sensor showed good performance in tracking the motion of both types of robots. The endurance of the sensor for the CAAR was limited by the sensor detaching from the material due to the low temperature of lamination of the sensor onto the robot body, originating from the temperature limitation of the 3D printed CAAR material. The performance of the sensor for the NWT showed excellent motion tracking over the entire tested range. This work has shown that the sensor is easily manufacturable and that the digital design can be adjusted to fit a wide range of soft robots. The understanding of the behavior of the sensor over a range of conditions and an extended period of use allows a soft robot's movement to be accurately tracked by the printed strain sensor.

# Chapter 1. Introduction

Continuum robotics is a growing field of robotics that uses the innate compliance of materials to allow the movement of a single continuous part as opposed to multiple connected parts. The field of continuum robotics has grown in size and capacity in recent years. This growth has led to continuum robots of smaller size and greater mobility than before. Continuum robots often are designed to experience strains of between 1% and 10% [17][22], with high strains being a possibility. Due to these high strains, continuum robots typically lack any sensing ability, which limits them to open-loop control systems. This naturally limits the applications for which they can prove useful. One application for which they are well suited is medical robotics. Continuum robots are being used to replace conventional surgeries with minimally invasive procedures.

A new procedure using a continuum robot may allow a skilled physician to destroy tumors in their office without surgery or anesthesia. The procedure is similar to a normal endoscopy, where the physician runs a small, flexible tube containing a camera down the patient's throat to examine the throat lining. In addition to a normal endoscopy, a physician uses a special endoscopic tool located at the tip of this tube. It is a single fiber that carries cell-destroying laser energy. By placing this fiber on the tumor and pulsing a laser through it the physician can kill the tumor without cutting it out. Early trials show improved recovery times for patients and reduced load on physicians.

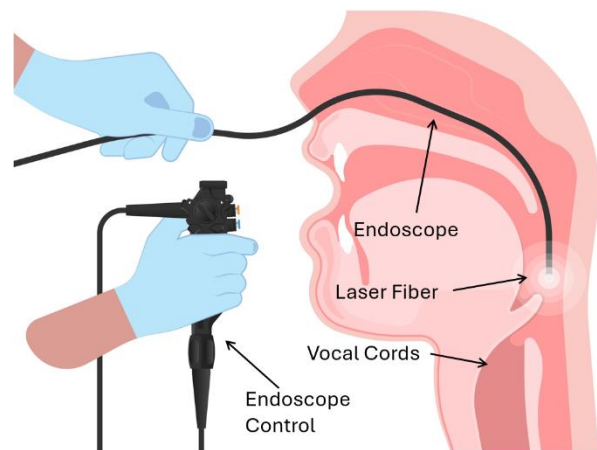


Figure (1.1) A laser fiber fitted to the end of an endoscope can destroy cancerous tumors in the vocal folds of a patient without the need for invasive surgical

Yet, there is a problem with this method. The physician has to touch a single fiber to a tiny tumor inside a patient's body while controlling a 3-foot-long tube that snaked its way through a patient's nose and throat. All while avoiding hitting healthy tissue with the laser. Imagine cleaning the inside of your kitchen drain with a toothbrush tied to a string. The

physician has to get everything lined up just right, and then, time the laser so it hits the tumor and not the patient's vocal cords. And of course, the patient has to stay perfectly still while the doctor wrestles with the endoscope. To reduce the strain on the physician, a novel system for controlling the laser fiber was developed [4]. This system uses a continuum robotic end effector called a Notched Wrist Tube (NWT) to move the laser fiber into position. The NWT is located on the tip of the endoscope and bends the laser fiber into position on a tumorous growth. Ideally, a computer controller would be able to adjust the finer movement of the NWT without direct input from the physician. However, there is currently no way for a computer to recognize the real-world position of the NWT. Adding the ability to electronically sense the shape of the NWT in real time to the system would make it possible to include closed-loop control of the laser fiber.

Adding position or shape sensing to continuum robots typically happens with either electromagnetic (EM) sensing, optical sensing, or resistive strain gauges. Electromagnetic sensing works by detecting the small changes in the magnetic field between a magnetic field generator and a magnetic sensor. EM trackers can be placed on a continuum robot, providing specific points for the EM tracking system to follow [27]. Electromagnetic sensing is a complicated process, with many separate parts. The Aurora EM Tracking system, a commercially available system developed by Northern Digital Inc. (NDI), consists of 4 parts. A Magnetic Field Generator that creates the magnetic field, the sensors that interact with that field, a Sensor Interface Unit that amplifies the signals from the sensors, and the System Control Unit that controls the field generator and collects the information. This system functions without requiring line-of-sight with the sensors, meaning that the sensors can be inside a patient, but the field generator and control systems can be outside the patient [28]. This is a unique advantage and means the system will not degrade at high strains.

Optical sensing is typically done with Fiber Bragg Grating (FBG) sensors. The sensors are placed on an optical fiber and measure changes in the wavelength of the light that passes through the optical fiber. That change in wavelength corresponds to changes in strain. FBG sensors can be small enough to integrate into continuum robots meant for minimally invasive surgeries. They are accurate and have high sensitivity. They are also stiff and are only useful for strains of less than 1% [28]. FBG sensors are sensitive to temperature as well, so any

surgical procedure would have to account for the changes in temperature that happen inside a patient [28].

Resistive strain gauges measure the change in resistance of a conductive material as that material is strained. These strain sensors have the benefit of being an easy measurement to record. The circuitry required to record resistance is far simpler than what is needed for EM or FBG sensors. While printed strain sensors can be made of many different materials [5], conventional strain gauges are far more limited in their construction. Generally, they are made of a metal foil that is cut in a thin serpentine pattern and sandwiched between insulated sheets [3][24]. The metal foil is the sensing component and its electrical resistance changes under strain. However, it can also change due to temperature changes. Due to this, conventional strain gauges are made from metals with low electrical variation caused by temperature changes. This makes them expensive. Also, these sensors are useful for only relatively small working strains [2][6], typically less than 1% [26], which limits its possible applications. They can be used for things like structural monitoring of building materials or aviation parts [2][25]. For applications that experience larger strains, such as continuum and medical robotics, there are printed resistive strain sensors.

Additive manufacturing techniques have been used to create a large variety of new strain sensors [8][11][21]. Sensors made in this fashion usually consist of a conductive medium that experiences changes to its electro-mechanical properties when it is placed under strain. Metal-polymer, carbon-polymer, and liquid metal composite inks are all being researched for the conductive material in printed strain sensors. These printed materials are stretchable, with some being stretchable up to 250% after printing [8]. They are all commercially available as

	Capable of Tracking	Cost	Temp Sensitivity	Max Strain
Fiber Bragg Grating	Total Curvature	High	High	>1%
Electromagnetic	Individual Points	High	None	N/A
Resistive Strain Gauge	Total Curvature	Low	Low	>1%
Printed Resistive Strain Gauge	Total Curvature	Very Low	Low	250%

Table (1.1) A table comparing the characteristics of various sensing methods for continuum robots used in medical robotics. Note that there is no maximum strain for EM tracking. Since it tracks individual points it is not affected by high strains.

printable inks, although they are marketed as stretchable conductors or resistors. Using these inks for strain sensing has not yet been thoroughly researched.

There are many methods to print these inks into strain sensors. Some, such as Digital Light Processing (DLP), are capable of intricate and high-resolution designs. The high cost of DLP means it is not easily available [8]. Stencil and screen printing are widely used and can create many sensors from a single mesh screen with a high throughput, but they require stencils and screens to be prepared ahead of time which slows down prototyping. Direct ink writing (DIW) printing is a convenient digital approach by which the sensors can be rapidly prototyped. DIW involves a conductive ink being deposited onto a stretchable substrate through a nozzle. Once dried and cured, the resistance of the printed material will increase when the substrate and printed material are stretched, in much the same way that the resistance of a conventional strain gauge sensor material will increase. Therefore, a strain sensor can be made by measuring and monitoring this change in resistance.

DIW printing generally requires precise tuning since small differences in the ink's properties, such as density or viscosity, can affect the final printed sensor [7][8]. This, and the slower nature of DIW printing, makes it difficult to produce large numbers of uniform sensors consistently. After printing, the printed materials require careful post-processing. The exact requirements depend on the type of ink and add complexity to the manufacturing process. However, once the process is understood, DIW can be used to design and prototype strain sensors for a number of applications due to their flexibility and the wide array of materials that can be extruded [8].

## **1.1. Literature Review and Knowledge Gap**

Printed strain sensors are not a new idea, and the literature on the creation is extensive [5][8][9][10][23][24][26]. [5][9][10][23] Are a collection of studies that built sensors containing carbon nanotubes or graphene. These studies do look at cyclic strain. However, they generally only test each sample for around 15 cycles. They make no calculations to determine linearity. When drift is mentioned, it is only briefly. [9][23] Both show sensors that display positive drift in some tests and negative drift in others. There is no discussion of the

causes of this drastic change in drift. [8] Provides an overview of printed strain sensors and various ways of printing them. It reviews over 50 different strain sensors reported in the literature. Despite encompassing many different works, there is no reporting on cyclic use or linearity. [24] Demonstrated the effect of a repeating serpentine pattern on gauge factor. The authors took advantage of planar serpentine structures to create a silver-based strain sensor with a high gauge factor and a strain range of 0 to 12%. They do look at cyclic use but only to show the survivability of the serpentine pattern. They focus their efforts on the geometry and not the characteristics of the printed material. [26] Developed a method of tuning the Gauge factor of a strain sensor based on microcrack formation created during post-processing. The sensor they used was graphene-based and could survive strains of 20%. However, the sensor was only tested for a maximum of 3 cycles, with no discussion of the sensor's drift or linearity.

There is too little research dedicated to extended cyclic use of these sensors. This is especially important for strain sensors used for measuring large strains because the strains are more likely to cause damage or plastic deformation. Studies that include cyclic strain tend to extend to only 10 or fewer cycles [23]. Most of the literature demonstrates the feasibility of a printed sensor over a few cycles of loading and unloading. However, most real-world applications would take place over at least dozens of cycles. The literature also consistently reports the gauge factors of the strain sensors but rarely explores how the gauge factor would change under different testing conditions. Drift is often not reported as it requires extended use to be noticed, and linearity is often not reported at all outside of commercially available sensors. An important aspect of choosing a sensor would be to know how the sensor will react to extended cyclic use, and if the sensor can be integrated into a device.

Some studies in the literature that do examine a significant number of cycles for DIW printed sensors and how different factors affect the sensor's performance are summarized in Table (1.2). These studies generally focus on silver and carbon composite materials. There is little research into inks that do not use carbon or silver at all. Some of these studies report sensors that show tremendous performance over a large number of cycles and deeply explore one factor that affects the long-term performance of that sensor. What none of these works do, is use the sensor as part of a continuum robotic system.

Summary of several recently reported DIW strain sensors and the testing applied to each sensor					
Printed Material	Max Strain	Factor(s) Tested	Gauge Factor (GF)	Number of Cycles Tested	Refs
Carbon Epoxy paste	10%	DIW Printing Parameters	up to 28.5	10,000	[29]
Graphene/AgNP	100%	Ink Composition	21.2-48.2	500	[30]
Ag NWs	10%	Max Strain	22-33	100	[31]
Ag-Pb paste	6%	Max Strain	1	250	[32]
Silica/ Ecoflex/ MWCNT	150%	Max Strain, Frequency	$1.4 - 2.5 \times 10^6$	15,000	[33]
Graphite oxide-PVDF composite	15%	Max Strain, Frequency	14.5	>3000	[34]
Silver Polymer Composite	4%	Max Strain, Strain Rate, Dwell Time	up to 21.06	50	This Work
Carbon Polymer Composite	4%	Max Strain, Strain Rate, Dwell Time	up to 3.69	50	This Work
Eutectic Gallium-Indium Liquid Metal (ELMNT)	4%*	Max Strain, Strain Rate, Dwell Time	up to 1.03	50	This Work

Table (1.2) A summary of several notable strain sensors reported in the literature that report cyclic loading. Factors Tested refers to the specific factor(s) that the work used to investigate the behavior of the sensor under cyclic loading.

\*ELMNT in can likely go much higher than 4%. This work only tests it to 4% strain.

## 1.2. Objectives and Scope

This work investigates the DIW printing of a silver polymer composite ink, a carbon polymer composite ink, and a eutectic gallium-indium ink for the purpose of strain sensing on continuum robots. The silver polymer composite and carbon polymer composite inks both are cured after being printed, turning them into a solid material. The gallium-indium ink is a eutectic mixture, meaning the combination has a lower melting temperature than the separate components. This ink remains a liquid while it is used for strain sensing.

After printing and post-processing, the printed materials will be tested to fully explore their behavior during cyclic strain in terms of gauge factor, drift, and linearity. The effect of max strain, strain rate, and dwell time on those critical characteristics will also be explored. Simple stretch testing of the printed sensors would not be sufficient, as it causes the material to sag as the TPU substrate is deformed and needs time to recover. This means the true strain is hard to determine during stretch testing. It is also unrealistic, as the sensor is designed to be attached to a solid object. This work will develop a novel method to test the printed material in order to eliminate the material sagging.

After investigating three different inks to how their performance changes when used under different conditions, one ink will be chosen to investigate how soft sensors can be used with continuum robotics to add sensing to these devices. Specifically, a concentric agonist-antagonist robot (CAAR) and a notched wrist tube (NWT). These continuum robots are flexible and operate by bending along the length of the robot. The CAAR is a 3D-printed robot with a diameter of 8 mm. After successfully integrating a sensor with the CAAR, this work will show that a sensor can also be integrated with a much smaller tubular robot, the NWT. The NWT is designed to control a laser fiber inside the vocal folds of a patient during an in-office surgical procedure. Accordingly, it is much smaller than the CAAR and made of nitinol. In completing this final task, this work will show the versatility of the printed sensor and demonstrate the value of the knowledge gained from this exploration.

## Chapter 2. Printing and Characterization of Behavior of Printed Strain Sensors

Three different inks were used to print the sensors in this work by DIW onto stretchable TPU substrates. They were a silver-based ink, a carbon-based ink, and a eutectic gallium-indium based ink.

A commercially available silver-filled stretchable conductor ink (ACI Materials SE 1109) was used to print the silver-based sensor. After printing, the ink is cured by heating at 140 °C in an oven for 5 minutes. The ink's good adhesion to TPU, high stretchability, and ease of printing made it ideal for this project. It also has a fast-curing time which contributed to our ability to rapidly build prototype sensors.

For the carbon-based sensors, a commercially available carbon filled stretchable conductor ink (ACI Materials SE 1502) was used. Much like ACI Materials SE 1109, it had good adhesion to TPU, high stretchability, and was easy to print with. After printing, the ink is cured by heating at 140 °C in an oven for 5 minutes.

ELMNT.ST (UES, Inc) is a eutectic gallium-indium based ink which is a liquid at room temperature. As a metal, it conducts well but its liquid form gives the ink unique properties that make it good for sensor applications. It is described as benefiting from low hysteresis (good recovery after stretching) and high stretchability. It adheres to TPU well and does not require post-print baking. It does need to be encapsulated to keep the liquid from smearing if touched and to prevent oxygen from reacting to the gallium particles, which increases resistance.

It is important to note that none of these printed materials are designed or marketed to be strain-sensing materials. The silver-based and ELMNT inks are marketed as highly stretchable electrical conductors (and indeed have an excellent combination of electrical conductivity and stretchability), while the carbon-based ink is marketed as a stretchable resistive ink. Nonetheless, the potential for these printed materials to be used as highly stretchable strain-sensing materials is being evaluated in this work.

All three of these inks are conductive and can be used for strain sensing. The silver and carbon inks are a composite of conductive particles in a non-conductive polymer matrix, in which the electrical conduction occurs by electrical percolation [1][18]. The conductive particles suspended in the ink act as the conductive elements. When the dried printed material is stretched, the matrix is stretched, and the conductive particles are pulled away from each other. The increased distance between conductive particles is what increases the resistance over the strained portion of the printed material. When the material returns to its original state, the particles get closer together and the printed material becomes less resistive. ELMNT.ST is much different. Since it is a liquid metal, the conductive particles are not separated like the silver or carbon particles are. Rather, the eutectic gallium-indium liquid acts as a conductive fluid. However, gallium reacts to oxygen which forms an oxide shell around particles of gallium. The oxide shell is not conductive, which means the material will not be conductive after printing. The material is made conductive by breaking the oxide shells surrounding the gallium particles. This activation can be done by compression or stretching. When printed onto a substrate that has a flexible but not stretchable backing layer for added rigidity during processing, peeling the backing layer off the substrate can also activate the printed ELMNT. Once activated the printed material becomes conductive. This material generally has a low response to strain. Thinner traces can improve the strain sensing of the printed material by taking advantage of the reduction in the cross-sectional area of the encapsulated trace. As the printed ELMNT.ST sensor is stretched the trace becomes thinner, increasing the measured resistance.

In order to use these printed materials in strain sensors, it is important to understand several critical characteristics of the printed materials, including total resistance, resolution, responsivity, static range, dynamic range, gauge factor, linearity, and drift. This paper looks at the last three - gauge factor, linearity, and drift, in the most detail. These three characteristics can be heavily influenced by cyclic use. Additionally, the sensor may be affected by the manner in which the cyclic strain is applied. This paper will look at three variables - maximum strain, strain rate, and dwell time, to determine their effect on the three chosen characteristics. Any strain sensor that is going to be applied for larger strains over multiple cycles would need to be used with a good understanding of how those three characteristics would change during the use of the sensor.

Gauge factor (GF) is a common way to quantify the response of a strain gauge. And is defined as the ratio of the relative change in its resistance ( $\Delta R/R_0$ ) to the strain  $\varepsilon$  applied to that sensor, as given in Equation 2.1.

$$GF = \frac{\Delta R/R_0}{\varepsilon} \quad (2.1)$$

A high gauge factor corresponds to a more responsive sensor and is generally more desirable. A sensor with a low gauge factor would be less useful in situations where there is considerable noise in the signal. However, some printed materials will experience a change in their gauge factor over multiple cycles or may have gauge factors that are dependent on strain magnitude or strain rate. These are important phenomena to understand because they have major implications for the relationship between strain and measured resistance.

The linearity of a sensor describes how uniformly the change in resistance matches the change in strain. Ideally, a sensor's resistance measurement would change proportionally to the applied strain through the entire applicable range of strain. To determine the linearity of the sensor, this work uses the Best Fit Straight Line (BFSL) method [13][19]. A line of best fit is found for the loading portion of the last cycle for each test. The largest deviation of the measured resistances from that line of best fit is the error. The % Error is given in Equation (2.2):

$$\pm \% Error = \left( \frac{R_m - R_{BF}}{R_{BF}} \right) \times 100 \quad (2.2)$$

$$Linearity = 100\% - \% Error \quad (2.3)$$

where  $R_m$  is the measured resistance at the point of maximum difference between  $R_M$  and  $R_{BF}$ , and  $R_{BF}$  is the resistance predicted by the best fit. Sensors with high linearity and low error will be more accurate and require less processing power to interpret results [13]. Minimizing the % Error, or understanding its causes, is a critical factor in connecting the measured resistance of the sensor to an unknown strain.

Finally, drift is the measure of how the sensor's initial resistance, or its resistance under no strain, changes over multiple uses. Large drifts can have a drastic impact on the resistance over repeated cycles. This work looks to identify different characteristics of a loading and unloading cycle that have a large impact on drift. Specifically, the maximum strain,

movement speed, and time between cycles all contribute to the drift that is observed over time. One cause of drift is plastic deformation [20]. During strain, both the printed material as well as the substrate can experience unrecoverable deformation that will permanently change the resistance of the sensor, even when the strain returns to 0%. For the printed silver and carbon materials the non-conductive polymer matrix undergoes plastic deformation. The ELMNT, being a liquid, does not experience plastic deformation in the same way. In this work, TPU is used as a substrate for each sensor, and the TPU can plastically deform as well leading to drift even in the liquid metal sensors.

In addition to plastic deformation, the TPU experiences hysteresis when stretched. Hysteresis is the delay in the recovery of a material after a reduction in strain. TPU, while stretchable, does not return instantly to its original length after being strained. This means that when the stretching is applied cyclically, the TPU will eventually recover along an “equilibrium path” which depends on the maximum strain the TPU has experienced [15]. This means the length of the TPU will recover differently depending on the maximum strain, strain rate, or number of cycles. This can cause some delay between a strain change and the resistance change, and that delay will be different depending on the mentioned factors. Given time to rest after each cycle, change should be recoverable. This is why the time between cycles, or dwell time, is worth being investigated.

During cyclic loading and unloading, there would be a delay between the end of a cycle and the start of the next cycle. During this dwell time, the TPU and printed material would have time to recover from the strain. However, most applications would not give a sensor enough time to fully recover from the hysteresis. Given a less-than-ideal recovery time, it is important to know how much of a change in the characteristics of the sensor is due to the lack of recovery and how the dwell time can be used to reduce the negative effects of cyclic loading. Given that the hysteresis of the substrate and the polymer matrix are present in the printed material, giving the sensor more time to recover would likely have a positive impact on the sensor’s characteristics. With that in mind, it also follows that the speed at which strain is added to the sensor would impact those characteristics as well.

Movement speed, or strain rate, is a measure of how quickly strain is added to the sensor. It is possible that there is a speed at which the rate of strain would match the recovery of the

TPU, and the sensor would not show any hysteresis from the movement. This hypothetical speed would be extremely slow, and it would not be feasible to move the sensor slow enough to negate the hysteresis. A better understanding of the effect of movement speed on the sensor would make the selection of the right inks for an applicable strain sensor easier. It would also help in understanding the recorded measurements as the resulting changes to the sensor could be predicted based on the sensor's movements.

Lastly, drift, gauge factor, and linearity will be affected by the maximum strain the sensor experiences during the cycles. The printed materials will suffer more plastic deformation at greater strains and the hysteresis effect is greater for larger strains than for smaller ones, as it takes more time for the material to recover. This generally leads to significant drift and is why it is hard to make accurate soft sensors for strains over 1%. Greater strains also do damage to the printed materials themselves. Each cycle has the potential to create small cracks in the polymer matrix [20][24]. Those cracks can reduce the number of particles that are close enough to be conductive once the printed material is brought back to the unloaded state. As the number of cracks grows, the printed material loses conductive pathways and the resistance increases. This effect should be reduced with liquid metal sensors because they are not solid, and the liquid would immediately fill any cracks. Cracking can cause significant changes to the sensor's critical characteristics. Liquid metal-based sensors should face less change because of the lack of cracking, but they will still have the hysteresis and deformation of the TPU substrate.

## **2.1 Methods and Materials**

The sensors were printed onto a stretchable thermoplastic polyurethane (TPU) substrate (Lubrizol Estane® FS H92C4P), which has a Shore hardness of 92A. This TPU serves as the base material of the sensor. It was chosen for good tensile hysteresis (good recovery after stretching) and good adhesion with the conductive ink. While still flexible and stretchable, this TPU was relatively easy to handle during printing and post-processing, because of the removable PET backing sheet.

Lubrizol Estane® FS HM70A71 TPU hot melt was used to adhere the sensor to ABS beams. It allowed the sensor to remain flexible after application and has a low melting temperature which allowed the sensor to be adhered without damaging the TPU substrate.

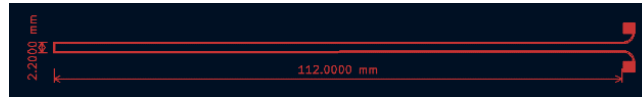


Figure (2.1) Dimensions of the design for the sensor that would be tested. The thickness of the printed lines depends on the nozzle size.

A simple sensor was designed (Figure 2.1) to measure the strain over a long but narrow space. Its sensing length was 112 mm and its width over the sensing area was 2.2 mm. At its base, it ended in two square pads. These pads were connected to electrical leads with copper tape. The transition from the sensing area to the pads is curved. The printer that was used tended to deposit extra ink at right angles and this was initially causing shorts at the base when the pads connected to the sensing portion at a 90-degree angle. The curved portion fixed this problem.



Figure (2.2) (From left to right) Silver, Carbon, and ELMNT sensors before attachment.

For the DIW printing of the sensor, a Voltera V-One direct write printer was used. The Voltera was simple to use and allowed rapid prototyping. TPU sheets with a PET backing sheet were clamped onto the print bed so the TPU was facing up. The sensor pattern was then

printed using a plastic nozzle with an inner diameter of 0.23 mm which was 0.10 mm over the TPU surface. A second pass was done to ensure complete continuity. The sensors printed with the ACI Materials silver and carbon inks were then baked in a 140 °C oven for 5 minutes. After baking the backing sheets were removed.

Unlike the silver and carbon sensors, the ELMNT sensors needed to be encapsulated to preserve the shape of the liquid metal and to prevent air from oxidizing the gallium particles. The sensors printed with the ELMNT.ST had copper tape applied to the pads before being encapsulated with a sheet of softer TPU. The substrate TPU had a hardness of 92A while the encapsulating TPU had a hardness of 75A. The sensor was placed in a 300 °F clamshell hot press for 5 minutes to encapsulate the ELMNT.ST in an airtight seal. The backing sheet was then removed which partially activated the sensor. The sensor was then stretched to 30% strain for 15 cycles at 15 cycles per minute in order to activate the ELMNT. The three sensors are shown in Figure (2.2)

To test the different printed materials, each one was used to print simple strain sensors (of the design shown in Figure (2.1)) onto TPU substrates, which were then attached using hot melt to ABS beams. Attaching the sensors to a solid object that is being strained provides a

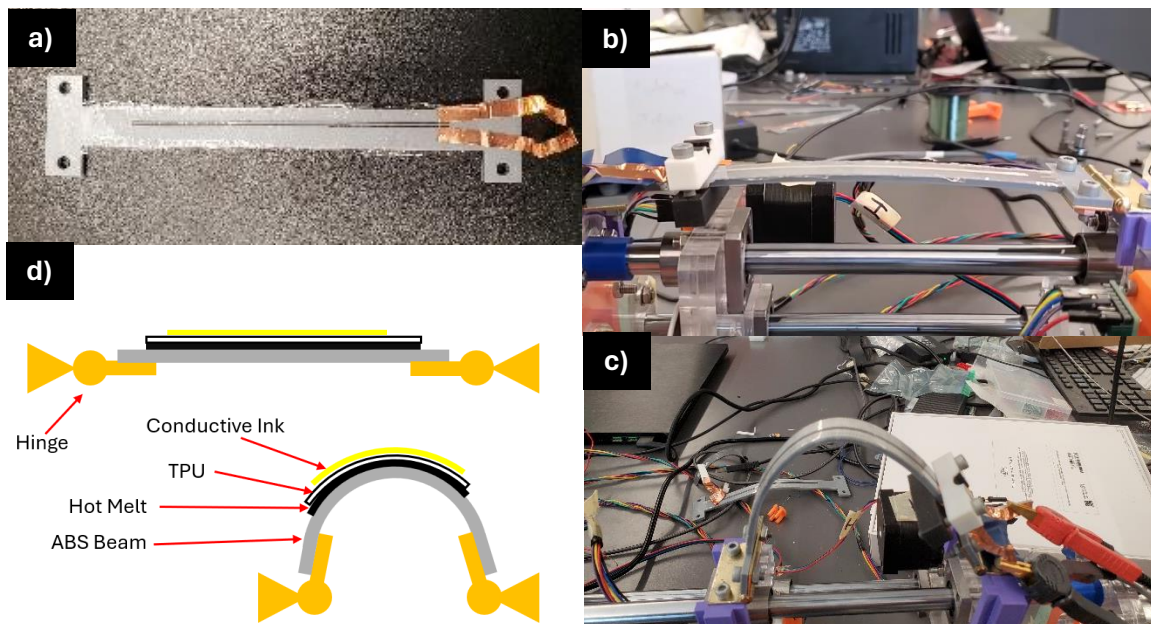


Figure (2.3) a) ABS beam with sensor. Copper tape connected the sensor to the resistance monitor b) beam at start of test. The beam sits flat between two hinges. The copper tape is clamped in place over the pads of the sensor. c) beam at 4% strain. d) Diagram showing how the sensor was tested.

realistic test for the sensors, as any application would include being attached to a stretching or bending object. Also, when tested without being mounted onto a solid object, the sensors would begin to sag after being stretched due to the hysteresis or permanent tensile set of the TPU. This sagging made it impossible to know the true length and strain of the sensor during testing. Bending was chosen as the main method of straining because it would simulate the movement of a soft robotic arm. The ABS beam was then pinned on both ends. The ends of the beam were pushed together, forcing the beam to bend in an arc, as shown in Figure (2.3). The strain on the beam was calculated with equation (2.4), where  $y$  is the distance from the neutral axis,  $\rho$  is the radius of curvature and  $\epsilon$  is the strain.

$$\epsilon = \frac{y}{\rho} \tag{2.4}$$

The beam that was used was 3 mm thick, so the distance from the neutral axis to where the sensor would be placed was 1.5 mm. The targeted maximum strain on the beam was 4%. Any higher strain risked breaking the beam. To achieve this, the beam was bent to a radius of curvature of 25 mm. This setup allowed control of the maximum strain, dwell time, and speed of the sensor.

	Max Strain	Strain Rate	Dwell Time
+	4%	1% per 12.5 seconds	5 seconds
-	2%	1% per 25 seconds	1 second

Run #	Max Strain	Strain Rate	Dwell Time	Gauge Factor	Drift	Linearity (%)
1	-	-	-			
2	-	+	+			
3	+	-	+			
4	+	+	-			

Table (2.4) Left: Table of the values assigned for each test. Right: Table of the 4 tests each sensor would be put through. The yield would be recorded for the Gauge Factor, Drift, and Linearity

An orthogonal array was used to plan the testing of the effect of three factors - maximum strain, dwell time, and strain rate. In the array “+” denotes a higher value, and “-“ denotes a lower value. Table 2.4 shows the specific values for each factor and the order in which the tests were run. Under this experimental design, each factor can be tested, as well as the interactions between factors, with four separate tests. In the first test, each factor is set to the lower value. In the following 3 tests, two factors were set to the higher value and one was set to the lower value. This way each possible combination (-++, +-+, ++-) is tested. Including all the tests, each factor has two tests set to the lower value and two tests set to the higher

value. Each test consisted of 50 cycles of loading and unloading, over which the electrical resistance of the strain sensor was recorded. The moment before a new cycle would start was marked as a critical point, and the slope of the line created by these critical points showed the drift.

## 2.2 Results

Some examples of the recorded tests are shown in Figure (2.5). There is one example for each of the three materials that were used. These examples help to see the difference between the different materials. Visually it is easy to see that the silver printed material has a very large positive drift (resistance increasing with strain cycles). Carbon shows a much smaller negative drift (resistance decreasing with strain cycles), while ELMNT.ST shows very little drift. Also, many of the tests showed a distinct change in the drift and gauge factor between the first several cycles and the remaining cycles. This was termed “warm-up” behavior and can be seen in the first few cycles of the ELMNT.ST test in Figure (2.5).

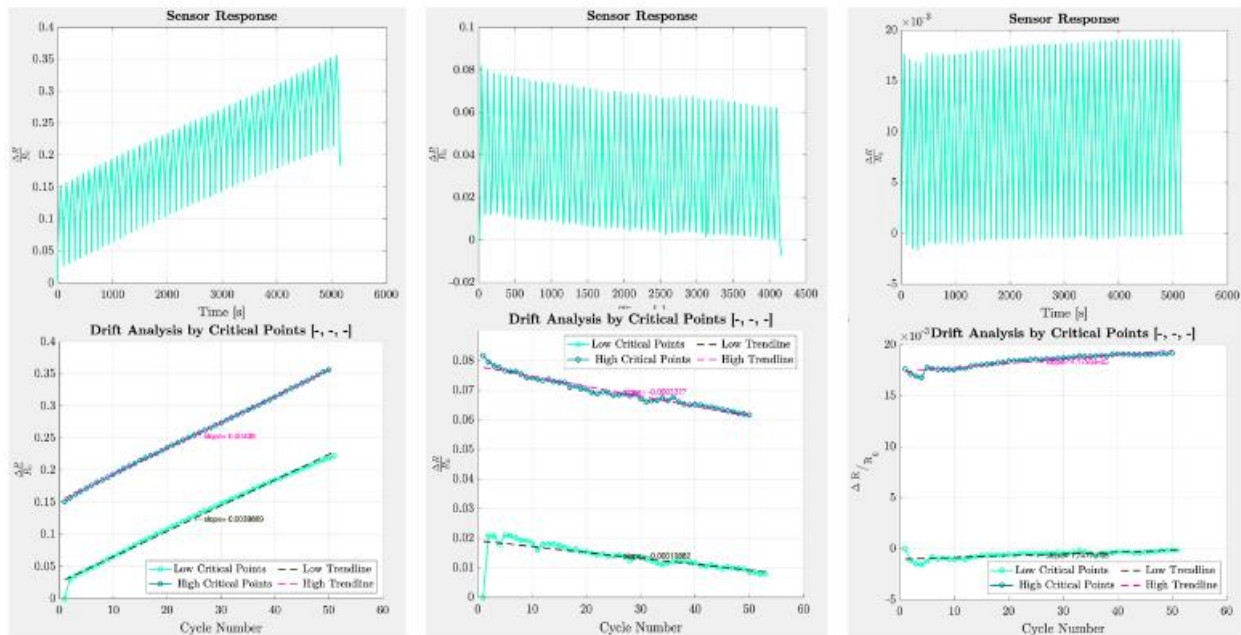


Figure (2.5) An example of the results of (from left to right) Silver (++-), Carbon (---), and ELMNT (++-) inks under 50 cycles of strain. The bottom results show the resistance at the critical points where the beam reached its minimum (green) or maximum (blue) strain.

The carbon printed material showed an interesting behavior at higher strains. As shown in Figure (2.6), at a 2% strain the carbon ink has one peak per cycle. However, at the 4% strain tests, a smaller peak appears during or after the unloading portion of the cycle. This behavior is known as a “double-peak” or “shoulder-peak” and appears in the literature as a common problem for carbon and graphene inks [5][9][10][23]. As it is a known phenomenon of some carbon inks, the effect was not investigated further. The double-peak hurts the linearity of the carbon sensor near the end of the unloading cycle and the beginning of the loading cycle.

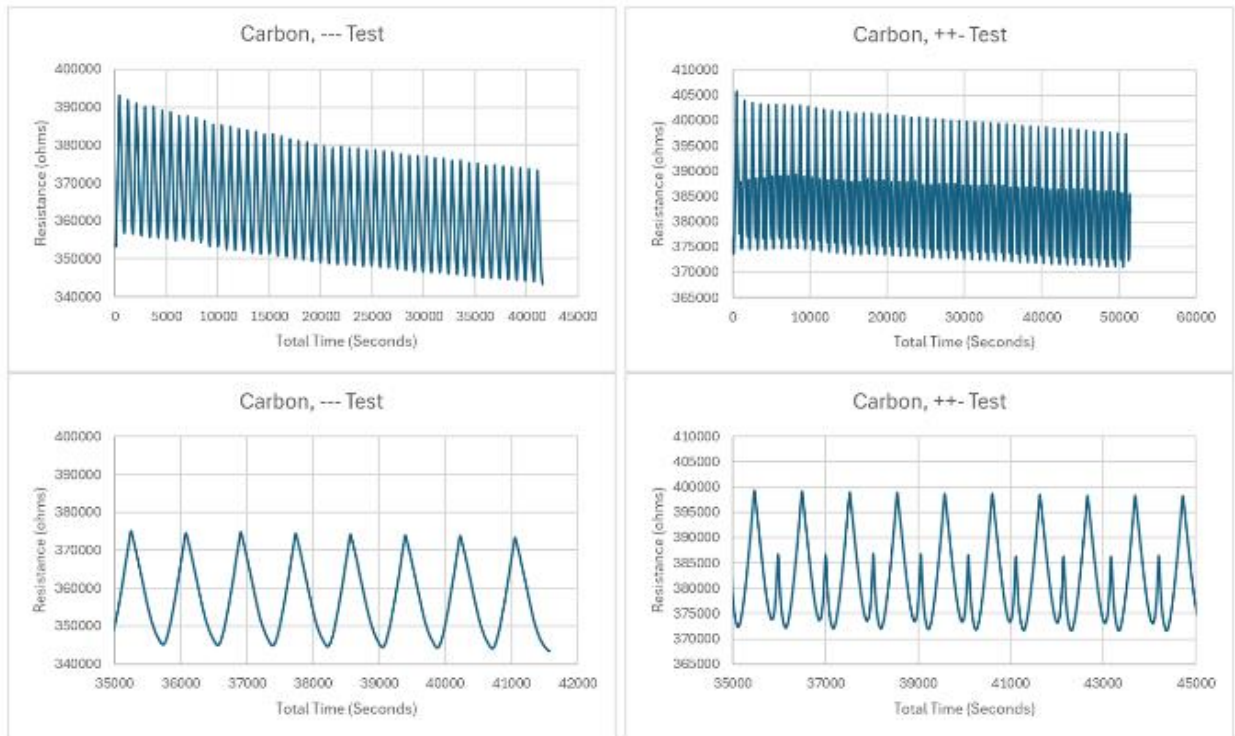


Figure (2.6) Top left: 50 cycles of the carbon sensor at 2% strain. Bottom left: a close-up view of several of the cycles at 2% strain. Top Right: 50 cycles at 4% strain. Bottom Right: a close-up view of several of the cycles at 4% strain. The double-peak can be seen here as a second, smaller peak that comes right after the larger, primary peak.

ELMNT also had some unexpected problems at first. The silver and carbon sensors were generally predictable after the first 10 cycles of a test. After the first 10 cycles, their drift would be fairly consistent until the end of the test. For the ELMNT, this was not the case. The drift would often be consistent for many cycles and then the resistance would suddenly jump or drop several Ohms. It occasionally would do this multiple times in one test. It was also common for the printed material to show an uncharacteristically heavy drift, both

positive and negative. To solve this problem different strategies for the activation of the material were tried, but the seemingly random behavior continued. During the stretch activation, the sensor did not display any of these troublesome behaviors. It was hypothesized that the attachment to the ABS beam was causing an issue with the sensor. A test was run with hot melt placed only under the tip and base of the sensor so that it was not under any of the printed portions of the sensor. This change solved the problem and showed that the hot melt adhesive may cause an issue with the liquid metal sensors. All ELMNT sensors were re-printed and tests with ELMNT were redone without the hot melt interfering with the sensor.

The gauge factor was calculated using the loading, or “Up” portion of the final cycle. The initial resistance was taken from the last reading before the cycle started and the final resistance was taken from the first reading after the cycle reached its peak. Drift was determined by finding the critical points where the strain had returned to 0% and calculating the line of best fit for those points. The slope of the line of best fit is taken as the drift in the sensor. This process can be seen in Figure (2.5). Of note, many of the samples that were tested experience a sort of “warm-up” period in the first few cycles where there is significant and non-linear drift. To avoid this initial warm-up period, the first 10 cycles are not used to determine the sensor’s drift. Linearity was calculated using the Best Fit Straight-Line method on the loading portion of the last cycle for each test. The resulting gauge factor, drift, and linearity for each individual test is plotted in Figures (2.7, 2.8, 2.9) along with the averages.

		Gauge Factor	Drift (( $\Delta R/R_0$ ) / Cycle)	Linearity (100% - %Error)
Silver	---	1.75	0.00097	99.34
	---	2.11	0.00137	99.63
	++-	4.80	0.02167	96.41
	++-	21.06	0.01252	82.40
Carbon	---	3.59	-0.00034	98.17
	---	3.69	-0.00045	98.51
	++-	1.65	0.00019	96.71
	++-	2.02	-0.00002	97.27
ELMNT	---	0.90	0.00001	99.80
	---	1.03	0.00002	99.80
	++-	0.75	0.00011	99.81
	++-	0.78	0.00001	99.81

Table (2.1) The resulting average yield from each test is shown here.

The average result for the three tests is reported in Table (2.1). In order to compare the printed materials, the drift, gauge factor, and linearity were plotted together in Figure (2.10). A close-up of zero on the X-axis is shown in Figure (2.11) in order to better show the largest clusters of data points. This figure shows the relatively close grouping of the carbon sensors compared to the silver. It also shows the effect that the later tests at higher strains had on the silver printed material as those tests had a far wider range of results.

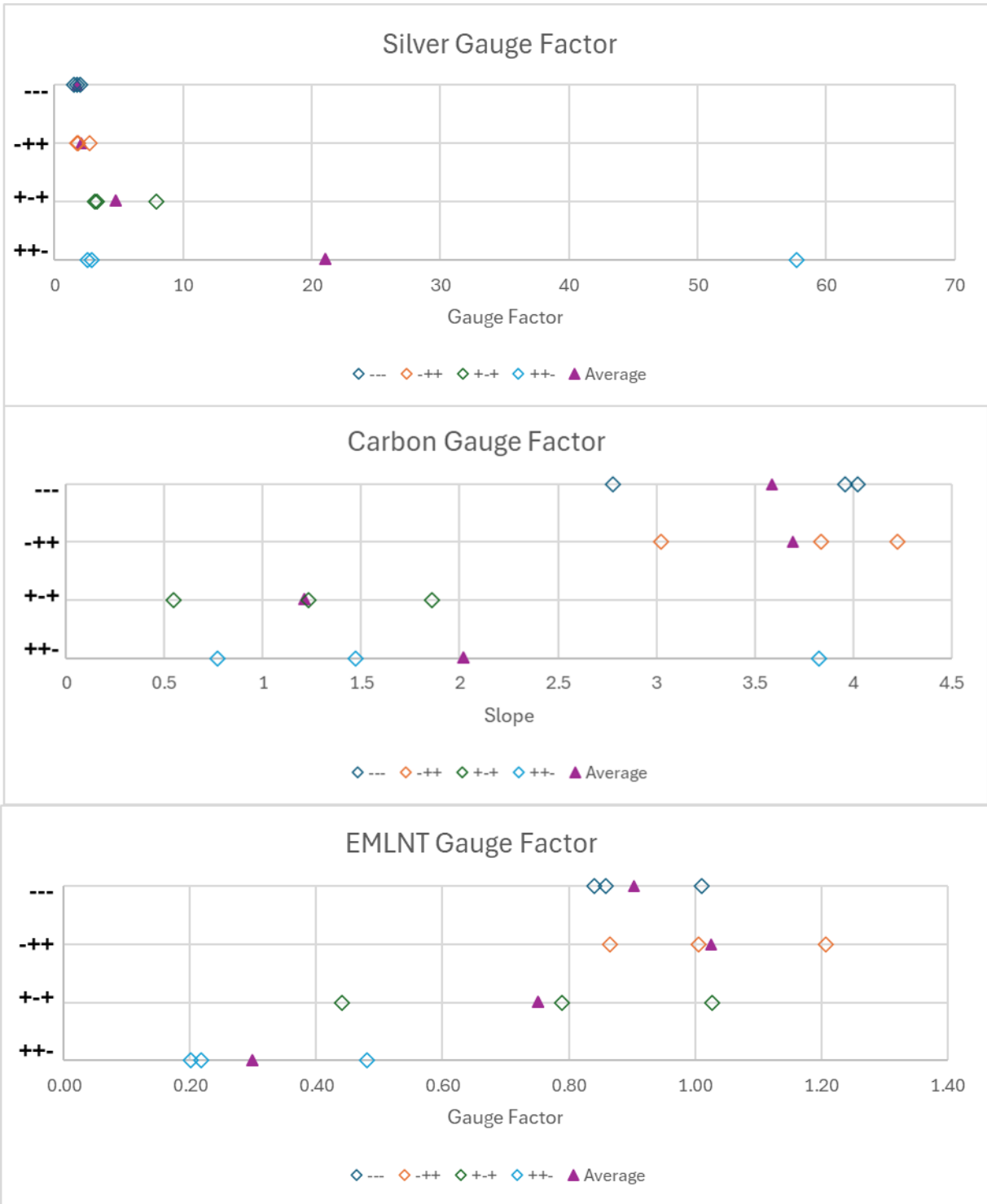


Figure (2.7) Each test was run three times. The Gauge Factor from those tests, along with the average, is plotted here under the corresponding printed material and test parameters.

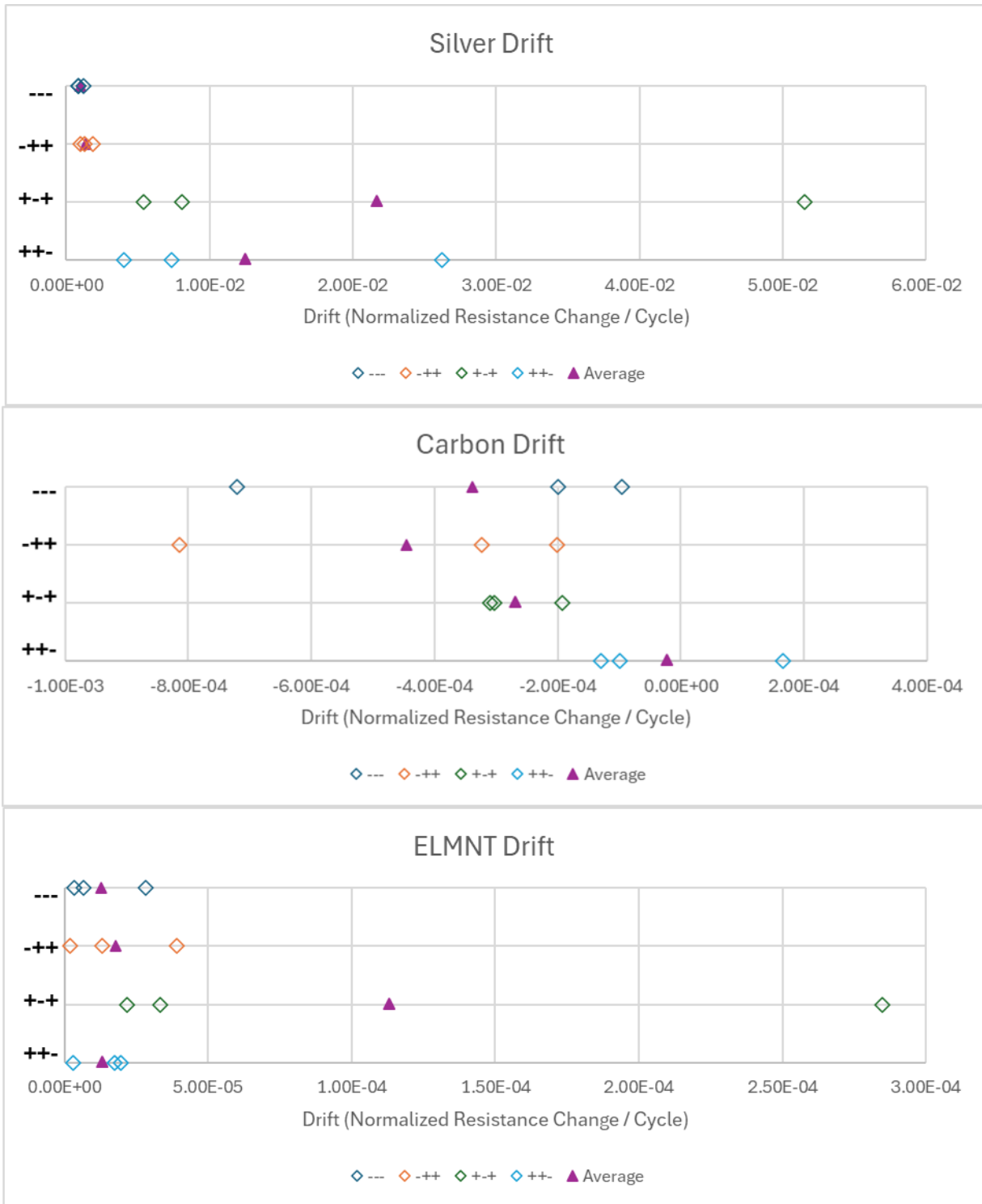


Figure (2.8) Each test was run three times. The Drift from those tests, along with the average, is plotted here under the corresponding printed material and test parameters.

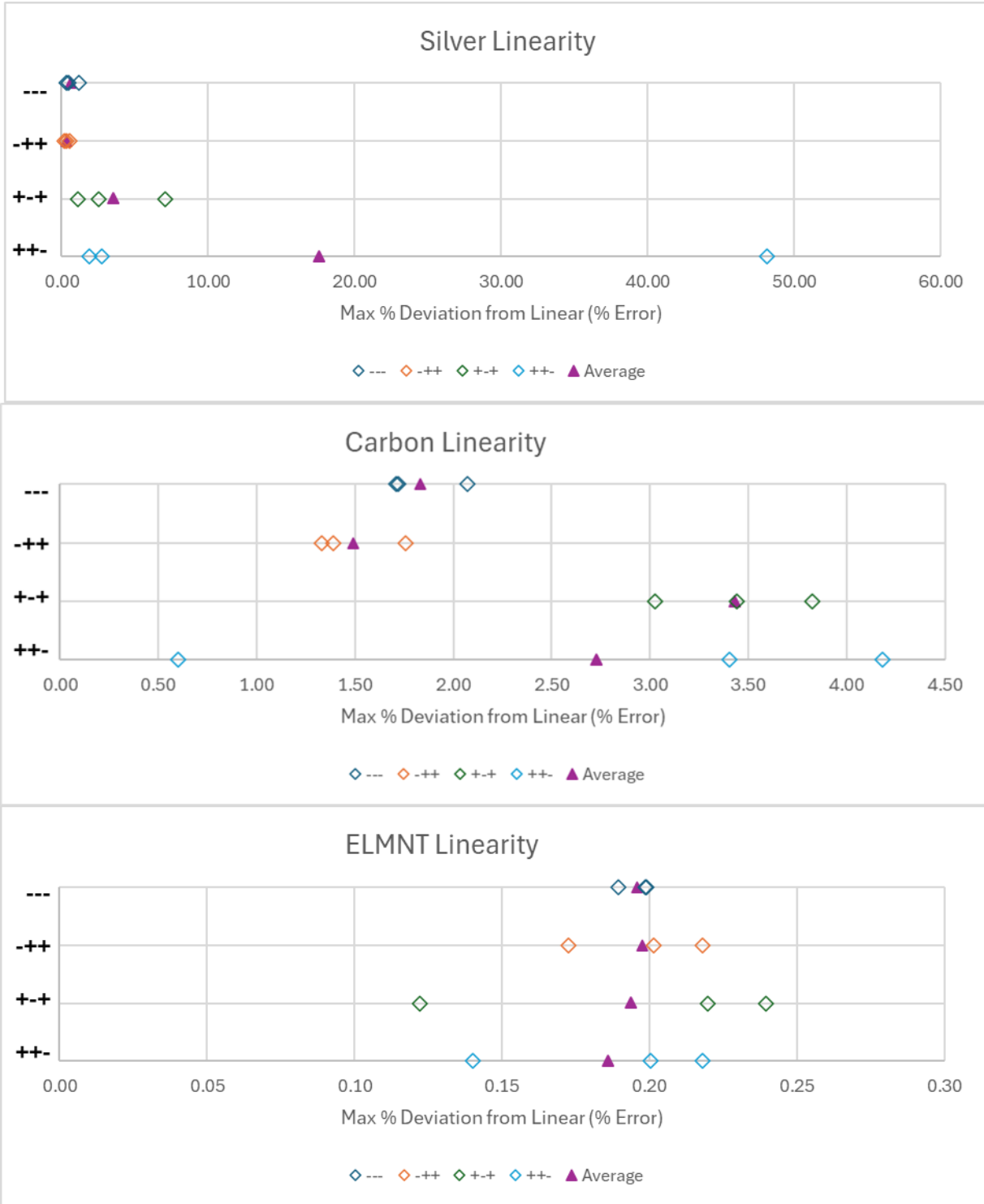


Figure (2.9) Each test was run three times. The Linearity from those tests, along with the average, is plotted here under the corresponding printed material and test parameters.

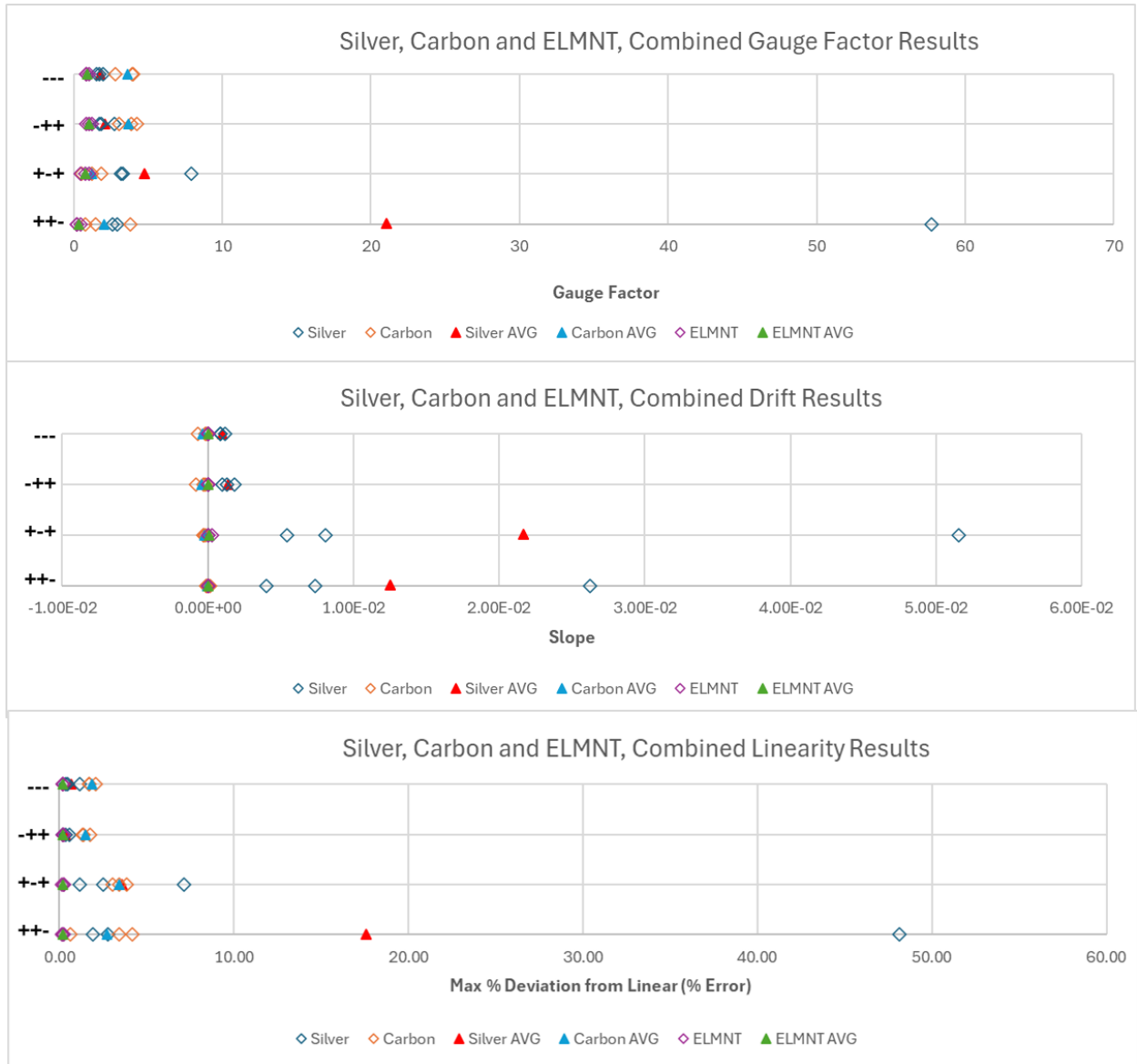


Figure (2.10) Each test was run three times for each ink. The result of every test is shown here.

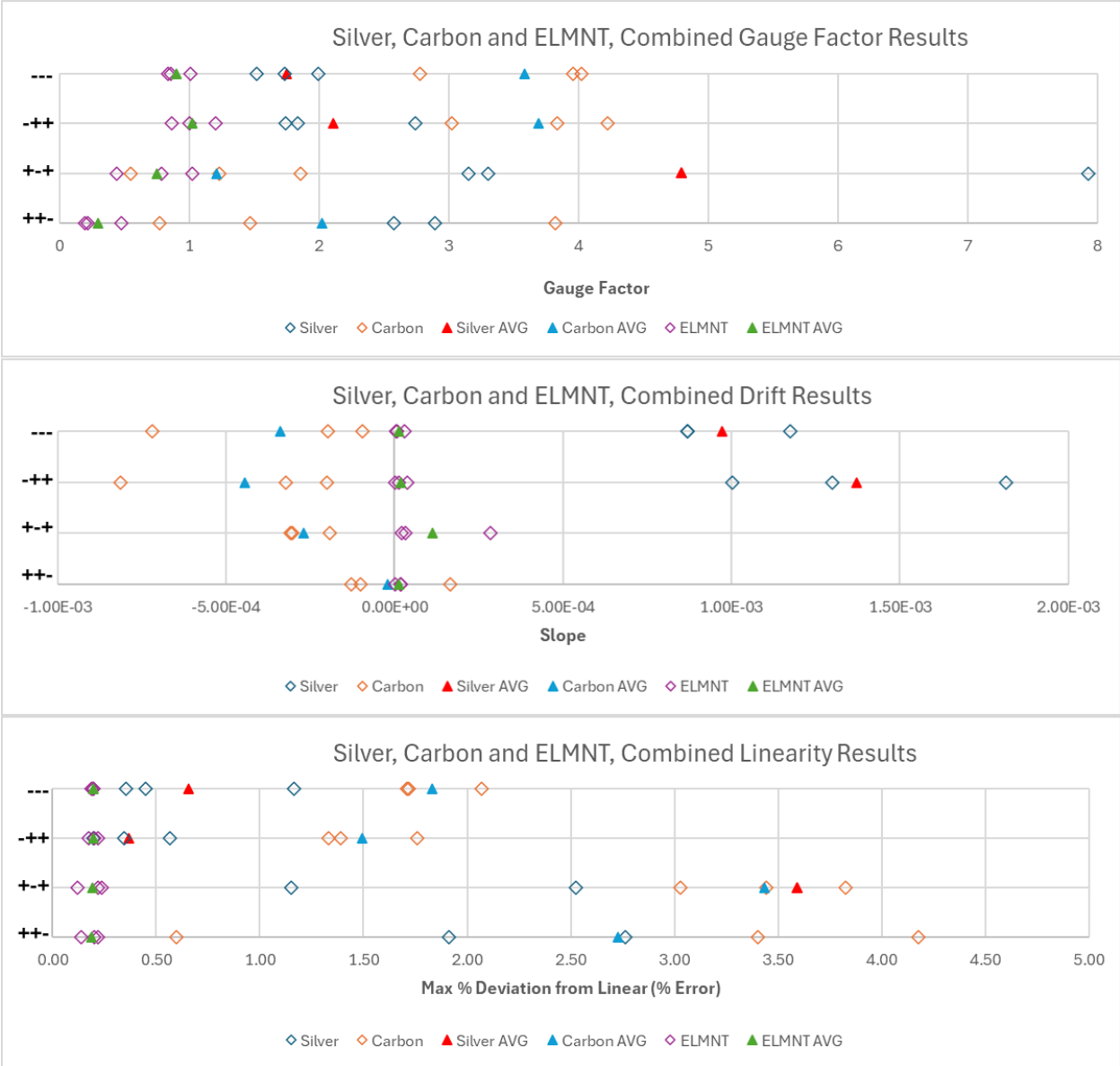


Figure (2.11) This is a zoomed-in version of Figure (2.10) which better illustrates the differences between the printed materials.

These results can be used to reveal some general trends about each printed material. Returning to the testing parameters, where tests marked with a “-“ have that parameter as the lower value and tests marked with a “+” had a higher value, the general effect of individual factors can be determined by subtracting the tests where that factor was at the lower or “-“ value from the tests with a higher value or “+”. This method of evaluating the effect of each factor allows more information to be gleaned from fewer tests, which saves considerable time. It is good for showing trends in the data but cannot provide quantifiable predictions. The method is shown in equation (2.4) and an example is shown in equation (2.5).

$$Effect\ Value = (PT_1 + PT_2) - (NT_1 + NT_2) \quad (2.4)$$

Where  $PT_1$  and  $PT_2$  are the Positive (+) tests,  $NT_1$  and  $NT_2$  are the negative (-) tests, and the effect value is a quantity to compare the effect of one factor with the other two. As an example, I will examine the effect that maximum strain had on the silver printed material gauge factor compared to the strain rate, and dwell time. From Table (2.1), the two positive tests for maximum strain (++ and ++-) averaged 4.80 and 21.06 of normalized resistance drift per cycle. The two negative tests for maximum strain (--- and -++) averaged 1.75 and 2.11 of normalized resistance drift per cycle. Using equation (2.5):

$$Effect\ Value = (4.80 + 21.06) - (1.75 + 2.11) \quad (2.5)$$

The Effect Value of the maximum strain on gauge factor is 22 normalized resistance drift per cycle. Doing the same process for the strain rate and dwell time gives effect values of 16.62 and 15.91, respectively. This shows that maximum strain is the largest factor behind the gauge factor for the silver printed material. The process was done for each material, test parameter, and critical criteria. The resulting effect values are reported in Table (2.2) along with a ranking of each of the parameter’s contribution to the change in each criterion.

		Gauge Factor		Drift ( $\Delta R/R_0 \cdot \text{Cycle Number}$ )		Linearity (100% - %Error)	
		Value	Rank	Value	Rank	Value	Rank
Silver	Strain	22.00	1	0.03185	1	20.1676	1
	Speed	16.62	2	-0.00875	3	13.7173	3
	Dwell	-15.91	3	0.00955	2	-14.2932	2
Carbon	Strain	-4.23	4	0.00106	4	1.6854	4
	Speed	1.10	5	-0.00042	5	0.1018	6
	Dwell	-0.89	6	0.00021	6	-0.7830	5
ELMNT	Strain	-0.88	7	0.00010	8	-0.0130	7
	Speed	-0.33	9	-0.00009	9	-0.0059	9
	Dwell	0.58	8	0.00011	7	0.0094	8

Top: Table (2.2) Calculated Effect Value for each factor and ink on each critical criterion. The factor is also ranked against each other effect value of that criterion.

Right: Table (2.3) A summation of the rankings for the Effect Values in simple terms. From table 2.2, rank 1 = Highest, rank 2,3,4 = High, rank 5,6 = Medium, rank 7,8 = Low, rank 9 = Lowest.

		Gauge Factor	Drift ( $\Delta R/R_0 \cdot \text{Cycle Number}$ )	Linearity (100% - %Error)
Silver	Strain	Highest	Highest	Highest
	Speed	High	High	High
	Dwell	High	High	High
Carbon	Strain	High	High	High
	Speed	Medium	Medium	Medium
	Dwell	Low	Medium	Medium
ELMNT	Strain	Medium	Low	Low
	Speed	Lowest	Lowest	Lowest
	Dwell	Low	Low	Low

## 2.3 Discussion

Interestingly, Table (2.2) shows a very small or negative value for the strain rate's effect on drift for each printed material. That suggests that increasing the strain rate may decrease the drift of the sensor, especially for ELMNT. It does seem surprising that increasing the strain rate would decrease the drift, but that was consistent for all three sensors. Future works can explore this relationship in more detail. The effect of maximum strain on drift is positive for all three sensors tested, suggesting that increasing the maximum strain will increase drift. Linearity and gauge factor are less consistent between sensors. The values differ between positive and negative

relationships depending on the printed material. The one constant between all sensors and almost all criteria is that the maximum strain has the largest impact, either in the positive or negative direction, of any factor. For the ELMNT sensor's drift, the dwell time was just slightly more impactful.

Table (2.2) makes it very clear that the ELMNT.ST is the most stable of the printed materials. Over 50 cycles, it has the lowest overall change to its gauge factor, lowest drift, and lowest change to its linearity. It also has the best linearity overall. Its main weakness is the low gauge factor. Compared to silver and carbon, ELMNT's gauge factor is more stable, but it is also a lot smaller. This could affect ELMNT's ability to accurately sense small strains and would require the sensing system (including the electronics used to measure the sensor) to have low noise in order to measure small strain changes.

The carbon printed material tended to have a large gauge factor at the smaller strains, but a smaller gauge factor for the higher strain tests. This small gauge factor was still larger than what would be expected for the ELMNT printed material. It was also in the middle between the silver and ELMNT when it came to performance. It had low drift that was actually in the negative direction, which was unique among the tested sensors. Its linearity was poor compared to the ELMNT and the best of the silver tests, but it was consistent for both low and high strains. There was also the issue of the double peak behavior on the down stroke that was unique among the tested sensors.

The silver printed material had a high gauge factor, but it varied heavily and was easily affected by the tests. The resistance drifted the most of all the printed materials, and at high strains, its linearity suffered. At low strains, its linearity was actually fairly good, but the large drift and unstable gauge factor would require significant processing power to make sense of in real-time.

Again, it is important to note that none of these inks were designed or marketed as a strain-sensing material, but they are being evaluated as such in this work.

## 2.4 Conclusion

For most strain-sensing applications in soft robotics, the ELMNT ink will be the best option. Low drift and high linearity make up for its small gauge factor. It performs well over extended cyclic use and can survive far higher strains than this work subjected it to. Lastly, like all the printed materials tested, its simple design makes it ideal for prototyping and the fact it can be screen-printed means it can be manufactured in large numbers. Under some specific applications, the carbon printed material may be more useful. Applications that require higher gauge factors at low strain and can manage poor linearity can use carbon over the ELMNT. The silver printed material would likely not make for a good strain sensor, and should only be used as a stretchable conductor, as it was designed for. For soft and continuum robotics, ELMNT.ST has proven to be the best choice for printed strain sensors.

## Chapter 3. Integrating Printed Strain Sensor on CAAR

In order to demonstrate how to turn the knowledge gained from the research into 3D printed strain sensors into continuum robotic sensors it was vital to apply such a sensor to a continuum robotic body. Such a robot would ideally operate under similar strains and have enough room to fit a sensor. A 3D-printed Concentric agonist-antagonist robot (CAAR) [14] fits these requirements. A CAAR is made of an outer tube with notches placed along the length of the tube leaving a spine along the length. An inner tube with a similar design runs through the outer tube with the inner spine on the opposite side of the outer spine. The tips of the tubes are fixed together. A CAAR is able to bend forward or back, creating a 3 degree-of-freedom tubular robot.

Since CAARs can be 3D printed, they can be made to any size. They can be made from a variety of materials including ABS and similar materials [14]. The strain along the spine of the CAAR can be controlled by the design of the tubes and by the motion. However, CAARs are still relatively new robots. They lack sensing abilities, and their behavior is not well enough understood for them to be deployed commercially. CAARs must be fully understood and capable of providing feedback to a controller. Originally designed for medical robotics, CAARs assist in the care of surgical patients and allow for less intrusive procedures.

### 3.1 Methods and Materials

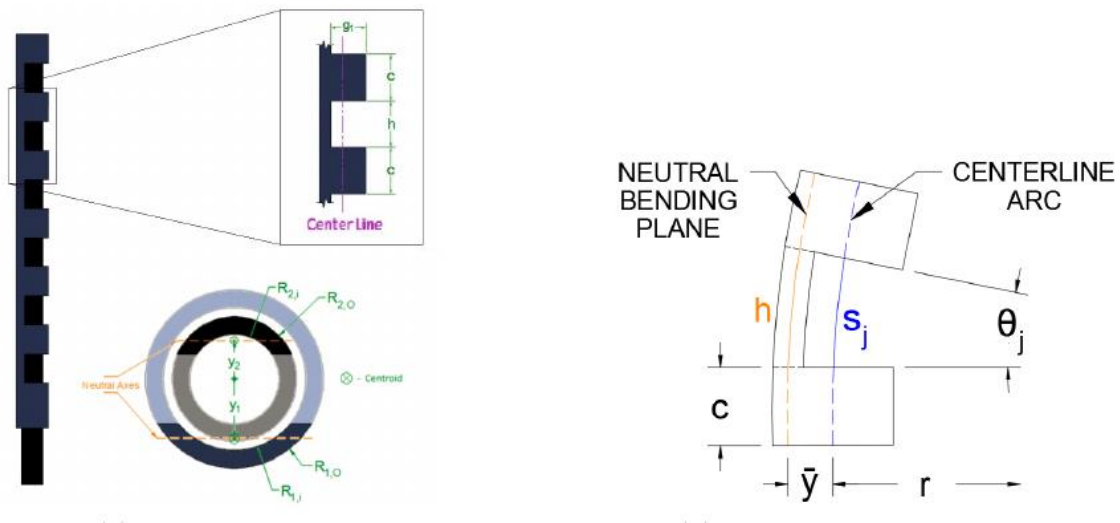


Figure (3.1) The dimensions of a CAAR. The CAAR used in this work had an outer diameter of 8 mm, wall thickness of 1.5 mm, cut depth ( $g$ ) of 6.4 mm, cut height ( $h$ ) of 7 mm, and gap height ( $c$ ) of 8 mm.

A 3D printed CAAR based on the design shown in Figure (3.1) was made with an outer diameter of 8 mm, wall thickness of 1.5 mm, cut depth (g) of 6.4 mm, cut height (h) of 7 mm, and gap height (c) of 8 mm. This gave a large enough spine to fit on a strain sensor of the same dimension as the one that had already been tested in the previous chapter. Based on the knowledge gained from the previous chapter, ELMNT ink was the obvious choice. Its high linearity and low drift was ideal for this application. A sensor with the same design as in the last chapter was printed and placed on the spine of the CAAR with the sensor's pads at the base of the CAAR and the tip of the sensor at the tip of the CAAR. The sensor covered the length of the spine. Hot melt was used just on the tip and base of the sensor. The sensor was attached to the CAAR in a clamshell hot press at 200 degrees Fahrenheit for 30 seconds. This melted the hot melt leading to a strong attachment at the base and tip. The TPU also pressed into the ABS allowing it to hold its place without the hot melt, although the adhesion is not as strong as with hot melt.

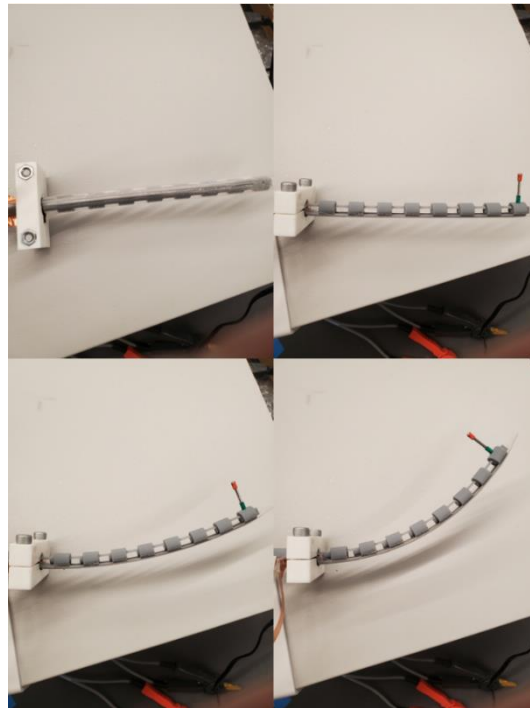


Figure (3.2) A CAAR with an ELMNT sensor attached on the spine undergoing bending strain up to

To test the sensor, the inner tube of the CAAR was pulled from 0 to 5 mm and back to 0. This caused the CAAR to bend inward and strain the sensor placed on the spine. This bending can be seen in Figure (3.2). At 5 mm of pulling length, the maximum strain placed on the spine of the CAAR is 0.714%. The CAAR would undergo this bending for 3 separate runs of 15 cycles with

each cycle taking about 50 seconds. The resistance of the sensor and the length the inner tube was pulled were recorded. After this test, the CAAR was then subjected to bending at set intervals. The inner tube was pulled at 1 mm intervals up to a total of 5mm and then back to 0mm. This interval test would show the sensor's responsiveness to smaller movements, along with the sensor's response to moments of rest at different strains. Once again, the resistance of the sensor and the length the inner tube was pulled were recorded.

### 3.2 Results

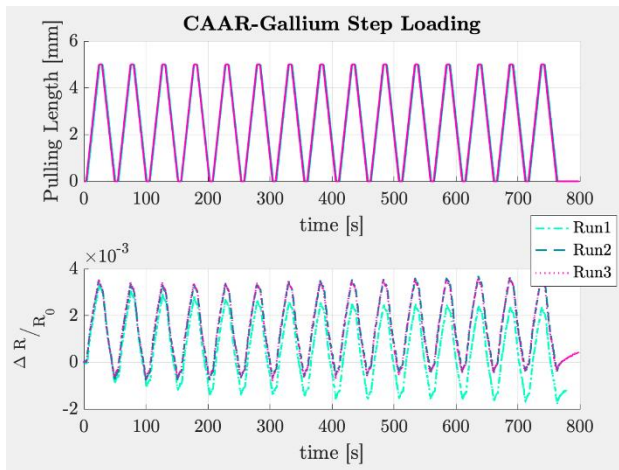


Figure (3.3) The resistance of the sensor as the CAAR is actuated. Run 2 and Run 3 are nearly identical.

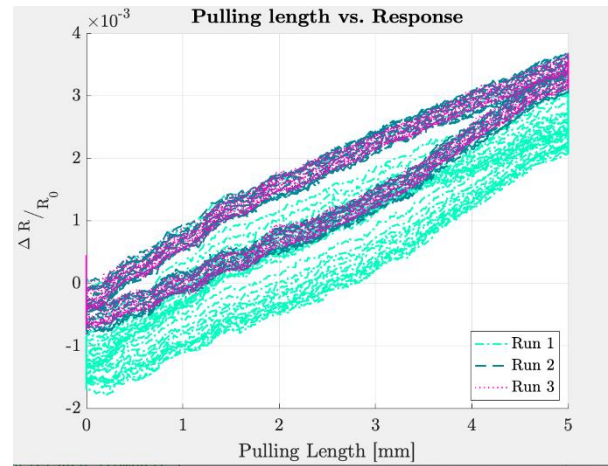


Figure (3.4) The resistance of the sensor with the actuation as the x-axis. The up-stroke has a higher resistance than the down-stroke.

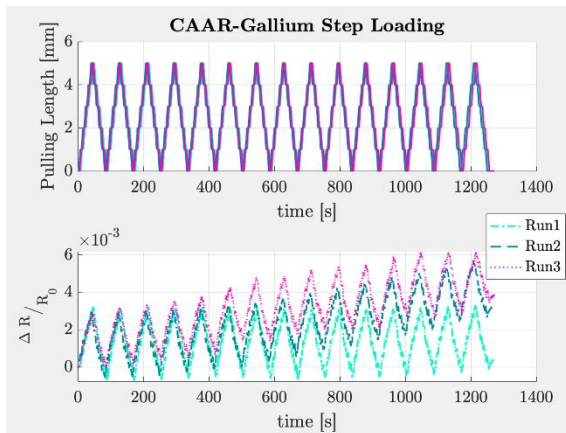


Figure (3.5) The resistance of the sensor as the CAAR is actuated in 1mm intervals.

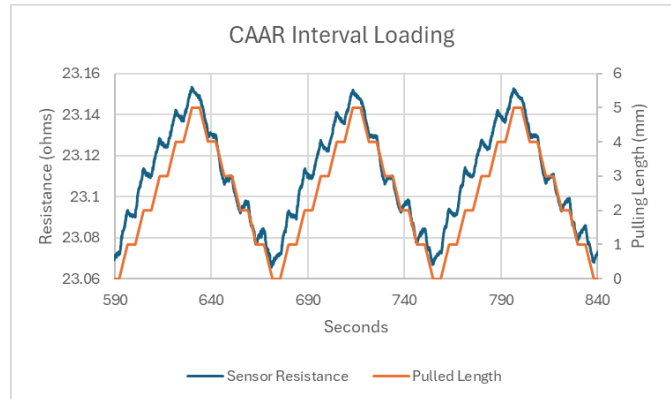


Figure (3.6) A close-up of three cycles of the first run from Figure (3.4).

Figure (3.3) shows the results of the first test. The recorded resistance is shown compared to the pulled length of the inner tube. The maximum strain at 5 mm of pull length was 0.714%. This gives a gauge factor of 0.47. The first run shows the “warm-up” behavior that commonly appeared in the testing from the previous chapter. The two subsequent runs are more consistent and show low drift and high linearity. Figure (3.4) shows the normalized resistance as a function of the pulling length. The shape of the sensor response is similar to the shape of the hysteresis response of TPU from H.J. Qi and M.C. Boyce [15]. This suggests that the TPU has a sizable impact on the response from the sensor.

Figure (3.5) shows the results from the interval loading test. In this case, the sensor had already been “warmed up,” so the first run did not have the normal inconsistencies early on. Instead, the second and third runs show far greater drift. This drift was caused by the middle portion of the sensor, the portion not attached with hot melt, becoming loose and no longer being attached to the CAAR. While the natural adhesion of the TPU to the ABS was strong at the beginning of testing, it lost that adhesion after dozens of cycles of use. Heating the TPU higher than 200 degrees Fahrenheit would have helped stick the sensor more firmly to the ABS material of the CAAR, but higher temperatures would have melted the ABS. The hot melt did not stay attached to the CAAR throughout all of the testing. The loss of adhesion caused the sensor to drift significantly. An in-depth look at three cycles from the first run is shown in Figure (3.6).

### **3.3 Discussion**

The sensor worked well for this application. The low drift of ELMNT shows very clearly and the high linearity is well demonstrated. Figure (3.3) shows the consistency of the sensor after the known “Warm-up” period, as Run 2 and Run 3 are nearly identical. The hysteresis of TPU does appear to affect the sensor to some degree, but the linearity of the ELMNT is still high enough to give an accurate account of the CAAR’s movement. To see how the sensor would respond to many stops and starts in one cycle, the interval test was done. The difference between the CAAR moving up, down, or staying is clearly seen in Figure (3.6). On the “up” stroke of the CAAR each interval consists of the CAAR being pulled by 1 mm to cause bending and strain on the sensor. As soon as the pulling is initiated, the recorded resistance shoots up and then plateaus when the pulling stops at the 1mm mark. At the pause in movement, the resistance ticks slightly downward until the next interval is started. This slight negative drift at the pause is likely caused

by the TPU settling after the movement. On the “down” stroke, it is much the same. However, during the pauses, the resistance ticks slightly upwards instead of downwards. This is likely not due to the TPU since the silver and carbon sensors tended to see the resistance tick downwards after recovering from strain. It appears that ELMNT experiences a slight rise in resistance in the time after the strain is reduced. The poor adhesion to ABS at low temperatures is concerning, especially considering the problems hot melt causes the sensor. However, improving that attachment method for longer endurance as well as investigating the rise in resistance after reducing strain can be explored in future works.

The Gauge factor was lower than what was expected based on the testing done in Chapter 2. It is possible that the curved shape of the tube is the reason. When the sensor is placed on both the CAAR and the NWT, the gap between the conductive traces running down the length of the sensor is placed on the middle of the spine, As shown in Figure (3.7). This means that the conductive traces themselves are slightly offset from the middle. On a flat surface, this would not have any effect. On a curved surface, this means the conductive part of the sensor would be closer to the neutral axis, and the strain on the sensor would be less than the maximum strain on the continuum robot. If this is the case the printed material was behaving predictably, but the placement on the robot was sub-optimal.

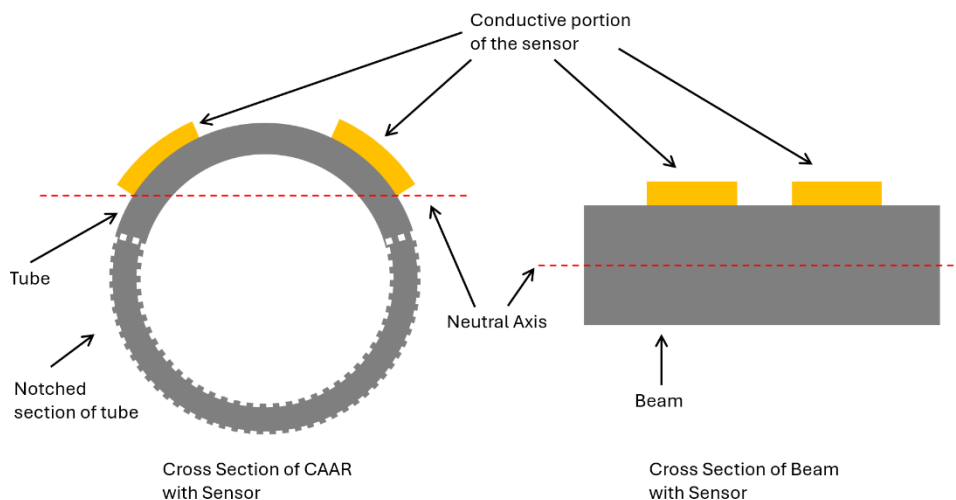


Figure (3.7) The placement of the conductive portion of the sensor on a tubular robot may affect the strain on the sensor. The closer to the neutral axis the printed material is, the less strain it will experience. On the flat beams tested in Chapter 2, this was not an issue. On a curved surface, it could be.

### **3.4 Conclusion**

The knowledge gained from testing different conductive printed materials has led to the development of a sensor that can be added to a continuum robot. This sensor can report the position of a continuum robot with high accuracy at both high and low strains. Combining this sensor with a capable processor would allow the CAAR, or other similar robot, to develop sensing abilities for closed-loop control. The CAAR was designed for surgical robotics, but it has a diameter of 8 mm. Most surgical applications would require much smaller robots. The goal became to integrate this sensor onto a far smaller platform.

## Chapter 4. Integrating Printed Strain Sensor on NWT

The main benefit of DIW printing is the rapid prototyping potential of the system. After successfully integrating a DIW strain sensor with a CAAR, the next challenge was to scale down the sensor to fit a much smaller robot. In this case, a Notched Wrist Tube (NWT, Figure (4.1)). An NWT is a straight, hollow tube with notches cut through the tube wall at intervals along the tube, leaving a spine that runs unbroken along the entire tube. A tendon is attached to the tip of the tube and runs down the center of the tube. When the tendon is pulled, the tube will bend in the direction of the notches cut into the tube [4][17][22].

This design is simple enough to allow it to be very small, down to around a millimeter in diameter. A nitinol notched wrist tube would be the platform for the sensor to be fit to.

The NWT to be fitted with a sensor in this project was 30 mm long with an outer diameter of 1.1 mm. This NWT was designed to be placed on the end of an endoscope to house a small laser fiber that would pulse high-powered laser energy on cancerous tumors for surgery on the vocal folds of a patient in a doctor's office. The NWT allows the doctor to have greater control over the position of the laser fiber tip once it is inserted into the patient's body. The hope is this will increase the doctor's ability to treat patients in an office setting and avoid costly surgeries. The main problem with this system is the physician is required to control the endoscope, the laser fiber, and the firing of the laser while trying to place the tip of the laser fiber on a tumor inside a patient's larynx. This is difficult to manage and leaves some areas out of reach of the treatment [4].

To simplify the procedure, our intention is to create a sensor that can detect the position of the laser fiber in real-time. This sensing ability can be fed back into a control system so the bending of the NWT could be controlled by a computer instead of the over-burdened physician. Such a sensor would have to be small enough to fit on the NWT, which had a diameter of 1.1

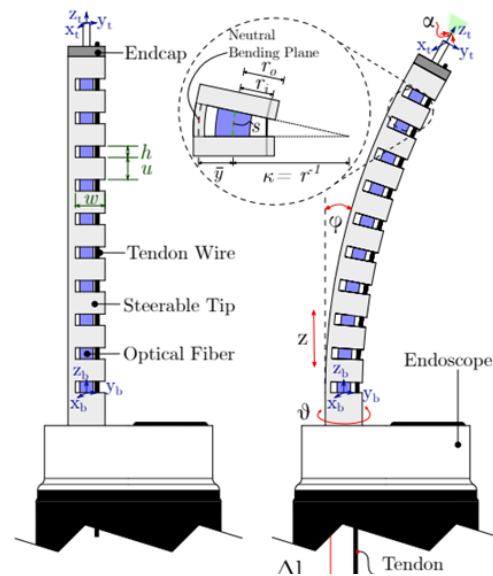


Figure (4.1) Example of a NWT placed at the end of an endoscope [4]

mm, and sensitive enough to give accurate position data. It also had to be robust enough to be used for the entire procedure.

## 4.1 Methods and Materials

A new sensor was designed to fit the NWT. Based on the excellent performance of the ELMNT ink, it was chosen again to be used in the sensor for the NWT and the Voltera V-One would be used to print this sensor. Using the same U-shaped design as with the CAAR required, the new design was made to be as narrow as possible but still ensure a gap between both of the 17 mm long legs. The final design is 0.7 mm wide over the sensing portion. This was just small enough to fit on the NWT. Aside from the difference in size, all other aspects of the sensor were the same as with the CAAR sensor.

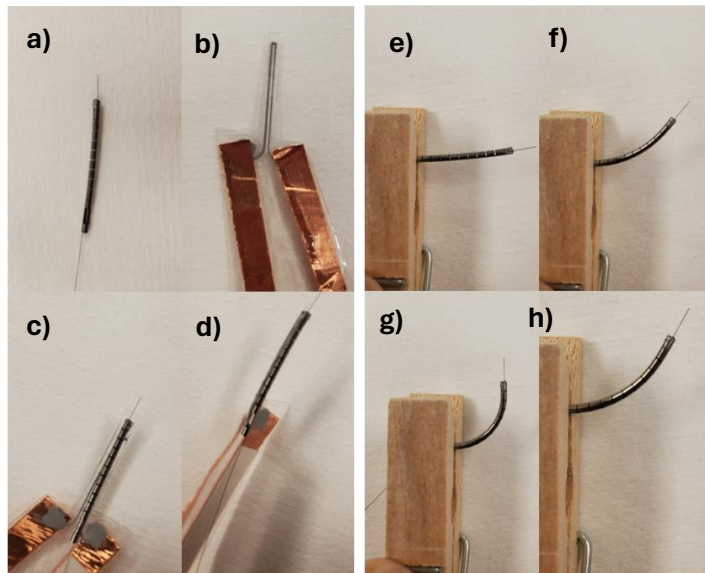


Figure (4.2) a) A NWT with tendon. b) The NWT sensor (unattached). c) NWT with sensor. d) NWT with sensor (side angle). e) NWT at zero position. f), g) h) NWT being bent by pulling the tendon.

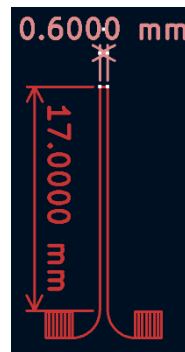


Figure (4.3) Dimensions of the design for the sensor that would be tested.

The sensor was attached to the NWT in a clamshell hot press with hot melt at the tip and base of the sensor. Since the NWT was made of nitinol it could survive more intense hot pressing than the ABS CAAR tested earlier. The hot press for the NWT was set to 300 degrees Fahrenheit. This helped the TPU form some attachment to the nitinol, although weaker than the hot melt's adhesion.

The NWT and sensor were tested to 50 cycles on a Yuasa Systems Desktop Model Endurance Test Machine with the stretching test jig. The NWT was clamped in place and the Endurance test machine pulled the tendon of the NWT to achieve cyclic bending and bending strains up to 10%. The NWT and sensor were tested at 15, 20, and 25 cycles per minute.

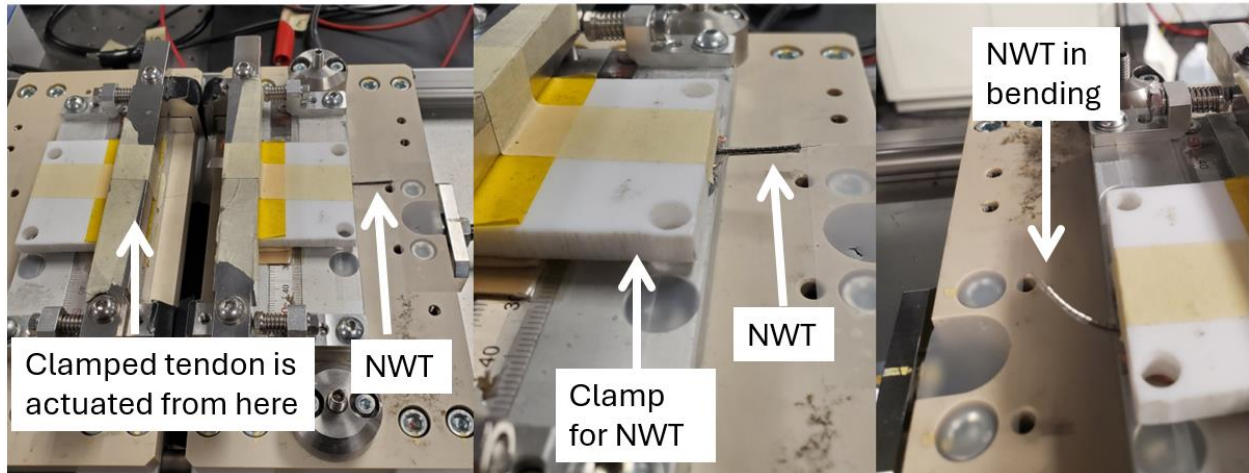


Figure (4.4) NWT clamped into the Yuasa Systems Desktop Model Endurance Test Machine with the stretching test jig. The tendon was clamped on the left side and pulled to induce cyclic bending.

## 4.2 Results

Figure (4.5) shows the recorded normalized resistance for the NWT sensor over 50 cycles of bending to the maximum bending strain and returning to the starting position. The last 10 cycles are shown in detail for each test. The readings show a drift of between 0.002 and 0.001 of

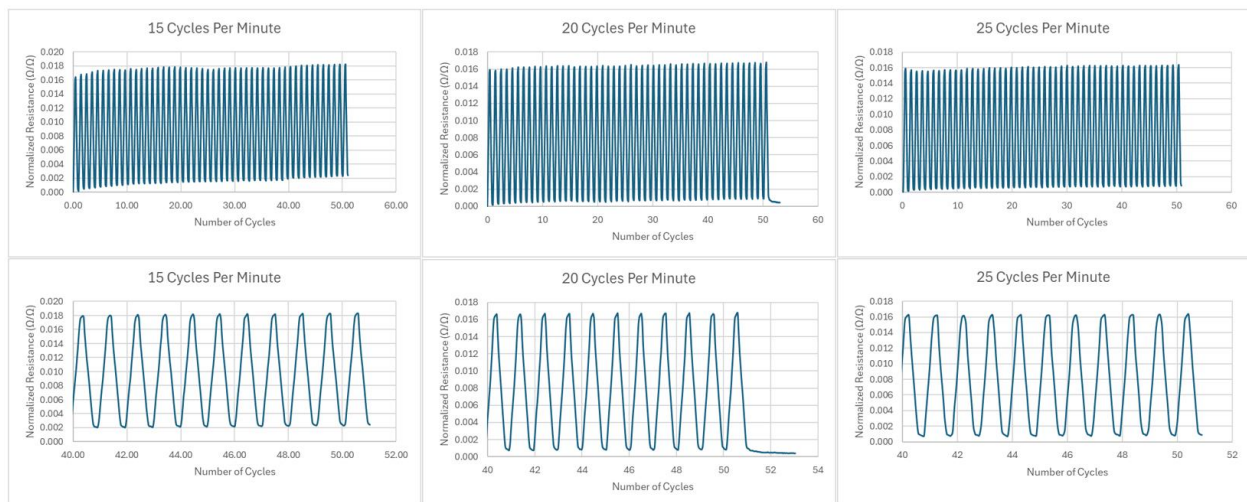


Figure (4.5) 50 cycles of bending for the NWT under different speeds (Top). The final 10 cycles from each test are shown in detail below the full test results.

normalized resistance over the 50 cycles. The gauge factor is between 0.16 and 0.18. Figure (4.6) shows the relationship of the strain to the normalized resistance returned by the sensor. The relationship is very linear for both the “up” and “Down” stroke.

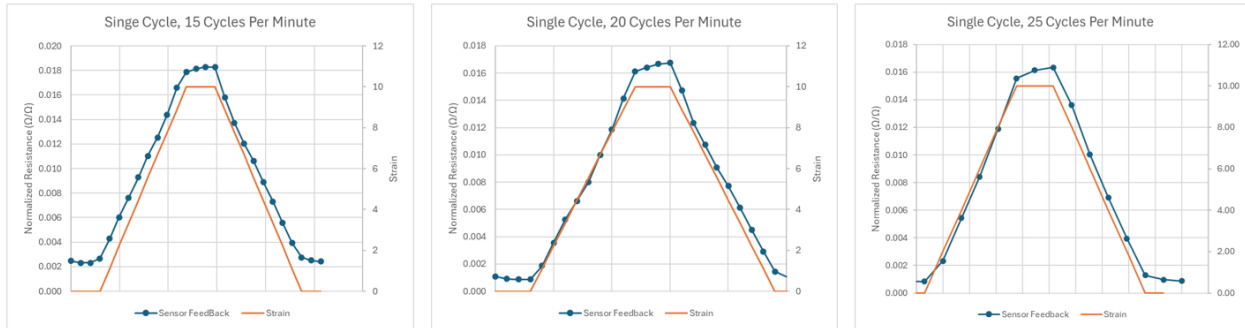


Figure (4.6) The last cycle of bending for the NWT under different speeds compared to the strain.

### 4.3 Discussion

The sensor performed well during these tests. The drift was higher during the slower 15-cycles per minute test than the faster 25-cycles per minute test. This was expected due to the results from the testing done in Chapter 2 of this work, as that testing showed higher speeds reduce drift slightly. The linearity of the printed material seems to be very high. The testing in Chapter 2 showed ELMNT had a linearity of 99.8 %. The testing with the NWT appears to match that accuracy. The gauge factor was substantially smaller during these tests than what was shown in Chapter 2. This was a surprising result. There were no changes to the printing of the sensor or the testing that explains the smaller gauge factor. While the testing in Chapter 2 showed ELMNT had a reduction in gauge factor at larger strains, it is unlikely that the higher strain in the NWT tests would result in such a large drop as was observed. It is possible that the difference in shape between the flat beam and the cylindrical tube had an effect on the gauge factor. The exact reason would have to be understood so it could be corrected, and the sensor could maintain a higher gauge factor while working with continuum robotics.

## 4.4 Conclusion

This strain sensor can accurately report the position of the tip of a notched wrist tube. It is small enough to fit on the NWT and not interfere with its operation. Its small gauge factor is a problem as it would be susceptible to noise interfering with its operation. The exact cause of the small gauge factor should be examined in future work. However, it is likely similar to the reason behind the smaller gauge factor seen during the CAAR testing (Figure (3.7)). Since the gauge factor is still larger than the drift, the sensor's performance is still very good. An ELMNT sensor could be used to allow an automatic controller to sense the position of the tube and move it without the operator's command. This can take some of the complexity out of the task of controlling the laser fiber on the end of an endoscope and improve patient outcomes for this application. In a broader scope, this type of sensor can be easily adapted to a broad range of soft and continuum robotics. The ease with which it can be prototyped and attached to a soft robot means it can quickly add sensing abilities to most projects.

## Chapter 5. Broader Impacts

The technology behind DIW sensors has the potential to impact more than just the medical field. DIW strain sensors can be incredibly small, or be scaled up for larger applications. This combined with their flexibility makes them ideal for soft robotic devices. Soft robotics is a growing field, especially in academia. One of the factors that limit their use in industrial or commercial sectors is the difficulty in controlling them. If we can build a system where a computer can know the real-world location of the notched wrist tubes during a medical procedure, then scaling that to a larger soft robot would be trivial. This would advance industrial and academic cooperation. Also, American industrial competitiveness would improve.

The flexibility of the soft robot matches the flexibility of DIW sensors. When paired together, they could give a soft robotic controller a way to track the robot's movements compared to the expected output, allowing the controller to recognize different things about its environment. For example, a robot arm with a soft gripping actuator could recognize objects by touch. This is an unheard-of capability in robotics. Placing the flexible strain sensors on a soft legged robot could tell the robot if one leg was stuck, giving the robot a chance to stop moving to save battery life, or try to free itself. This would give robotic engineers new ways to solve problems that, traditionally, soft robots have had to work around.

Strain sensors could show a computer where the appendage it controls is in the real world, but strain sensors could work the other way around. If embedded into the fabric of a glove, the strain sensors could be placed over the fingers, providing digital feedback of the wearer's movements. The wearer could use their fingers to control a robotic hand, for example.

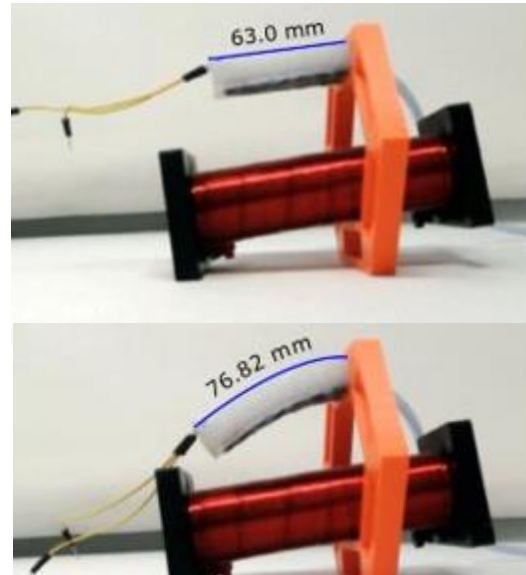
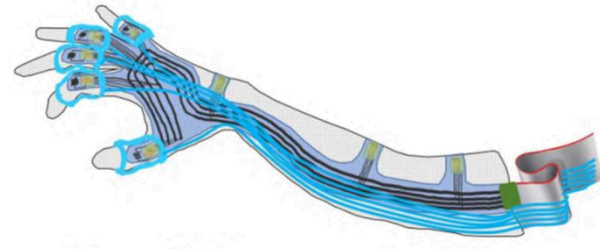


Figure (5.1) A soft robotic finger bends when air pressure is applied. Adding sensing to soft rubber would be a useful tool for engineers.

This could be used for controlling robotic arms, virtual reality or telework. The same system could be used in occupation therapy to track a patient's range of motion in their joints.



There are a lot of potential applications for the types of sensors, but the applications can be separated into

Figure (5.2) A glove with strain sensors embedded in the fabric could be used to collect data or control a robot.

two categories. Applications that give a user a new way to control a device, and applications where a computer is given some control of a device. In both cases there are some cases where this technology could cause problems. In the case where the human is controlling some device, most often that control will be with body worn sensors. This would be very convenient, and it would make controlling something like a robotic arm feel very natural. The problem is humans were not designed to control robotic arms. If the user lost focus or became fatigued, they could not set the controller down. It would be attached to them and moving the device with every one of their movements. A sneeze could result in a large, solid robotic arm moving uncontrollably. In situations where the arm is surrounded by people or important equipment, this could be disastrous. It is already the standard to use caution around robotic arms because they can behave unpredictably. They would be even less predictable when mirroring a human's arm motions.

For applications where a sensor feeds directly into a computer's control, the consequences of a singular hiccup from a human would be less serious. In this case, the problems could arise when the human user grows to trust the computer's control. To bring back the surgical example, if a doctor grew over-reliant on the computer to do the work, it would be natural to lose focus on the task at hand. This could be disastrous for the patient entrusting the doctor with their care. Designers must take care to include safeguards to keep users engaged with their tasks when utilizing strain sensing controllers.

The broad use for resistive, flexible, stretchable strain sensors coupled with their ease of manufacture make them easy targets for integration with existing robotic technology. The research into this topic will improve the well-being of medical patients, improve the economic competitiveness of the United States, and allow for opportunities to partner academia with

industrial stake holders. Once fully developed designers will have added capabilities at their disposal. The full extent of possibilities will be limited by the creativity of future designers.

## Chapter 6. Conclusion

The growing field of soft and continuum robotics requires the growth of compatible soft sensors. These sensors need to be available for researchers to prototype and experiment with. There is no easy “one size fits all” solution to soft sensing as flexibility of design and rapid prototyping is important to the labs building these types of robots. 3D printed sensors are able to fill this gap in capability but struggle to maintain both performance and stretchability.

The first chapter investigated the properties of three different sensors. It showed the strengths and weaknesses of each ink and was crowned a clear winner in the ELMNT.ST liquid metal ink. The silver ink was too easily affected by cyclic use, and its characteristics varied a lot based on the variables maximum strain, strain rate and dwell time. It also had a lot of variability between data points from the same test and was generally less consistent than the other printed materials tested. The carbon ink was less volatile than the silver ink, but it was still heavily affected by the maximum strain, which would limit its use in continuum robotics. ELMNT stood out for its low drift and high linearity. Its gauge factor was consistent, but also the lowest of the printed materials tested. This would require the system utilizing an ELMNT sensor to have low noise. For the purpose of integrating a soft strain sensor into a continuum robot, ELMNT was the best option.

The second and third chapters of this work help to prove this point. Both the CAAR and the sensor that was attached to it were made “in-house.” The sensor was designed to fit the CAAR and could show the movement of the robot through the change in resistance. This allows robots already in development to gain sensing abilities and increases the applications they could be used for. The sensor that was added to the NWT was designed and built in the same way that the one for the CAAR was. The dimensions of the sensor were just changed to fit the smaller robot. Once again, the sensor was able to show the movement of the robot over an extended period of use. The ease at which the sensor was changed to fit the smaller robot shows the customizability of the sensor.

This report does not answer every question about DIW strain sensors. Questions remain about how the geometry of the sensor might affect the critical criteria. Finding better means of attaching the sensor to soft robots is also worth of future research. The attachment methods used

in this work would not work for a soft robot made of silicone, for example. Exploring different substrates would also be beneficial, as the hysteresis of TPU causes some problems with the sensor. This report does, provides a framework by which other sensors can be tested and compared. When combined with future research this will increase the reach of direct ink write printed soft strain sensors.

## References

- (1) Ameli, Aboutaleb, et al. “A facile method to increase the charge storage capability of polymer nanocomposites.” *Nano Energy*, vol. 15, July 2015, pp. 54–65, <https://doi.org/10.1016/j.nanoen.2015.04.004>.
- (2) Anderson, Nickolas, et al. “Highly sensitive screen-printed strain sensors on flexible substrates via ink composition optimization.” *Sensors and Actuators A: Physical*, vol. 290, 1 May 2019, pp. 1–7, <https://doi.org/10.1016/j.sna.2019.02.028>.
- (3) Bao, Minhang. “Introduction to MEMS devices.” *Analysis and Design Principles of MEMS Devices*, 2005, pp. 1–32, <https://doi.org/10.1016/b978-044451616-9/50002-3>.
- (4) Chiluisa, Alex J., et al. “Light in the larynx: A miniaturized robotic optical fiber for in-office laser surgery of the vocal folds.” *2022 IEEE/RSJ International Conference on Intelligent Robots and Systems (IROS)*, 23 Oct. 2022, <https://doi.org/10.1109/iros47612.2022.9981202>.
- (5) Christ, Josef F., et al. “3D printed highly elastic strain sensors of multiwalled carbon nanotube/thermoplastic polyurethane nanocomposites.” *Materials & Design*, vol. 131, 5 Oct. 2017, pp. 394–401, <https://doi.org/10.1016/j.matdes.2017.06.011>.
- (6) Kervran, Y., et al. “Microcrystalline silicon: Strain gauge and sensor arrays on flexible substrate for the measurement of high deformations.” *Sensors and Actuators A: Physical*, vol. 236, 1 Dec. 2015, pp. 273–280, <https://doi.org/10.1016/j.sna.2015.08.001>.
- (7) Li, Xiaotian, et al. “Direct-ink-write printing of hydrogels using dilute inks.” *iScience*, vol. 24, no. 4, 23 Apr. 2021, p. 102319, <https://doi.org/10.1016/j.isci.2021.102319>.
- (8) Liu, Haodong, Hongjian Zhang, et al. “3D printed flexible strain sensors: From printing to devices and signals.” *Advanced Materials*, vol. 33, no. 8, 14 Jan. 2021, <https://doi.org/10.1002/adma.202004782>.
- (9) Liu, Hu, Jiachen Gao, et al. “Electrically conductive strain sensing polyurethane nanocomposites with synergistic carbon nanotubes and graphene bifillers.” *Nanoscale*, vol. 8, no. 26, 27 May 2016, pp. 12977–12989, <https://doi.org/10.1039/c6nr02216b>.
- (10) Liu, Hu, Yilong Li, et al. “Electrically conductive thermoplastic elastomer nanocomposites at ultralow graphene loading levels for strain sensor applications.” *Journal*

- of Materials Chemistry C, vol. 4, no. 1, 24 Nov. 2016, pp. 157–166,  
<https://doi.org/10.1039/c5tc02751a>.
- (11) Liu, Sijun, and Lin Li. “Ultrastretchable and self-healing double-network hydrogel for 3D Printing and strain sensor.” *ACS Applied Materials & Interfaces*, vol. 9, no. 31, 25 July 2017, pp. 26429–26437, <https://doi.org/10.1021/acsami.7b07445>.
  - (12) Liu, Xuehui, et al. “Self-healing strain sensors based on nanostructured supramolecular conductive elastomers.” *Journal of Materials Chemistry A*, vol. 5, no. 20, 19 Apr. 2017, pp. 9824–9832, <https://doi.org/10.1039/c7ta02416a>.
  - (13) Misron, Norhisam, et al. “Effect of inductive coil shape on sensing performance of linear displacement sensor using thin inductive coil and Pattern Guide.” *Sensors*, vol. 11, no. 11, 3 Nov. 2011, pp. 10522–10533, <https://doi.org/10.3390/s111110522>.
  - (14) Oliver-Butler, Kaitlin, et al. “Concentric agonist-antagonist robots for minimally invasive surgeries.” *SPIE Proceedings*, 3 Mar. 2017, <https://doi.org/10.1117/12.2255549>.
  - (15) Qi, H.J., and M.C. Boyce. “Stress–strain behavior of thermoplastic polyurethanes.” *Mechanics of Materials*, vol. 37, no. 8, Aug. 2005, pp. 817–839, <https://doi.org/10.1016/j.mechmat.2004.08.001>.
  - (16) Sun, Hao, et al. “An ultrasensitive and stretchable strain sensor based on a microcrack structure for motion monitoring.” *Microsystems & Nanoengineering*, vol. 8, no. 1, 29 Sept. 2022, <https://doi.org/10.1038/s41378-022-00419-6>.
  - (17) Swaney, Philip J., et al. “Design, fabrication, and testing of a needle-sized wrist for surgical instruments.” *Journal of Medical Devices*, vol. 11, no. 1, 21 Dec. 2016, <https://doi.org/10.1115/1.4034575>.
  - (18) Ukshe, Alexander, et al. “Percolation model for conductivity of composites with segregation of small conductive particles on the grain boundaries.” *Journal of Materials Science*, vol. 55, no. 15, 19 Feb. 2020, pp. 6581–6587, <https://doi.org/10.1007/s10853-020-04408-w>.
  - (19) “Understanding Linearity.” *AE Sensors*, [aesensors.nl/assets/uploads/2016/05/Understanding-Linearity.pdf](https://www.aesensors.nl/assets/uploads/2016/05/Understanding-Linearity.pdf). Accessed 12 Apr. 2024.
  - (20) Yeo, Joo Chuan, et al. “Flexible and stretchable strain sensing actuator for Wearable Soft Robotic Applications.” *Advanced Materials Technologies*, vol. 1, no. 3, 6 May 2016, <https://doi.org/10.1002/admt.201600018>.

- (21) Yin, Xiang-Yu, et al. “3D printing of ionic conductors for high-sensitivity wearable sensors.” *Materials Horizons*, vol. 6, no. 4, 15 Jan. 2019, pp. 767–780, <https://doi.org/10.1039/c8mh01398e>.
- (22) York, Peter A., et al. “A wrist for needle-sized surgical robots.” 2015 IEEE International Conference on Robotics and Automation (ICRA), 22 May 2015, <https://doi.org/10.1109/icra.2015.7139428>.
- (23) Zhang, Rui, et al. “Strain sensing behaviour of elastomeric composite films containing carbon nanotubes under cyclic loading.” *Composites Science and Technology*, vol. 74, 24 Jan. 2013, pp. 1–5, <https://doi.org/10.1016/j.compscitech.2012.09.016>.
- (24) Zhang, Suoming, et al. “Fully printed silver-nanoparticle-based strain gauges with record high sensitivity.” *Advanced Electronic Materials*, vol. 3, no. 7, 3 May 2017, <https://doi.org/10.1002/aelm.201700067>.
- (25) Zhao, Yinming, et al. “Dependance of gauge factor on micro-morphology of sensitive grids in resistive strain gauges.” *Micromachines*, vol. 13, no. 2, 10 Feb. 2022, p. 280, <https://doi.org/10.3390/mi13020280>.
- (26) Neilson, Joseph, et al. “Graphene-based transparent flexible strain gauges with tunable sensitivity and strain range.” *ACS Applied Nano Materials*, vol. 6, no. 23, 22 Nov. 2023, pp. 21763–21774, <https://doi.org/10.1021/acsanm.3c03967>.
- (27) Dore, Alessio, et al. “Catheter navigation based on probabilistic fusion of electromagnetic tracking and physically-based simulation.” 2012 IEEE/RSJ International Conference on Intelligent Robots and Systems, 20 Oct. 2012, <https://doi.org/10.1109/iros.2012.6386139>.
- (28) Shi, Chaoyang, et al. “Shape sensing techniques for Continuum Robots in minimally invasive surgery: A survey.” *IEEE Transactions on Biomedical Engineering*, vol. 64, no. 8, 27 Aug. 2017, pp. 1665–1678, <https://doi.org/10.1109/tbme.2016.2622361>.
- (29) Guo, Zhiyang, et al. “High-precision resistance strain sensors of multilayer composite structure via direct ink writing: Optimized layer flatness and interfacial strength.” *Composites Science and Technology*, vol. 201, 5 Jan. 2021, p. 108530, <https://doi.org/10.1016/j.compscitech.2020.108530>.
- (30) Kwon, Sung-Nam, et al. “Direct 3D printing of Graphene Nanoplatelet/silver nanoparticle-based nanocomposites for multiaxial piezoresistive sensor applications.”

Advanced Materials Technologies, vol. 4, no. 2, 10 Dec. 2018,  
<https://doi.org/10.1002/admt.201800500>.

- (31) Mohammed Ali, Mohammed, et al. “Printed strain sensor based on silver nanowire/silver flake composite on flexible and stretchable TPU substrate.” *Sensors and Actuators A: Physical*, vol. 274, 1 May 2018, pp. 109–115, <https://doi.org/10.1016/j.sna.2018.03.003>.
- (32) Nassar, Habib, et al. “Multi-material 3D printed bendable smart sensing structures.” *2018 IEEE SENSORS*, 27 Oct. 2018, <https://doi.org/10.1109/icsens.2018.8589625>.
- (33) Tang, Zhenhua, et al. “Coaxial printing of silicone elastomer composite fibers for stretchable and wearable piezoresistive sensors.” *Polymers*, vol. 11, no. 4, 11 Apr. 2019, p. 666, <https://doi.org/10.3390/polym11040666>.
- (34) Zhang, Mingchao, et al. “Sheath–core graphite/silk fiber made by dry-meyer-rod-coating for wearable strain sensors.” *ACS Applied Materials & Interfaces*, vol. 8, no. 32, 5 Aug. 2016, pp. 20894–20899, <https://doi.org/10.1021/acsami.6b06984>.